A&A 639, A136 (2020)
https://doi.org/10.1051/0004-6361/202038137

Astronomy & Astrophysics

The Fornax Deep Survey with VST

IX. Catalog of sources in the FDS area with an example study for globular clusters and background galaxies*

Michele Cantiello[1], Aku Venhola[2], Aniello Grado[3], Maurizio Paolillo[4,5], Raffaele D'Abrusco[6], Gabriella Raimondo[1], Massimo Quintini[1], Michael Hilker[7], Steffen Mieske[8], Crescenzo Tortora[9], Marilena Spavone[3], Massimo Capaccioli[4], Enrica Iodice[3,7], Reynier Peletier[10], Jesús Falcón Barroso[11,12], Luca Limatola[3], Nicola Napolitano[13,3], Pietro Schipani[3], Glenn van de Ven[14], Fabrizio Gentile[4], and Giovanni Covone[4,3,5]

[1] INAF Osservatorio Astr. d'Abruzzo, Via Maggini, 64100 Teramo, Italy
e-mail: michele.cantiello@inaf.it
[2] Astronomy Research Unit, University of Oulu, Pentti Kaiteran katu 1, 90014 Oulu, Finland
[3] INAF – Osservatorio Astr. di Capodimonte Napoli, Salita Moiariello 80131, Napoli, Italy
[4] Dip. di Fisica "E. Pancini", Universitá di Napoli Federico II, C.U. di Monte Sant'Angelo, Via Cintia, 80126 Naples, Italy
[5] INFN, Sez. di Napoli, Via Cintia, 80126 Napoli, Italy
[6] Center for Astrophysics | Harvard & Smithsonian, 60 Garden Street, 02138 Cambridge, MA, USA
[7] European Southern Observatory, Karl-Schwarzschild-Str. 2, 85748 Garching bei München, Germany
[8] European Southern Observatory, Alonso de Cordova 3107, Vitacura, Santiago, Chile
[9] INAF – Osservatorio Astr. di Arcetri, Largo Enrico Fermi 5, 50125 Firenze, Italy
[10] Kapteyn Astronomical Institute, University of Groningen, PO Box 72, 9700 AV Groningen, The Netherlands
[11] Instituto de Astrofśica de Canarias, Calle Vía Láctea s/n, 38200 La Laguna, Tenerife, Spain
[12] Depto. Astrofísica, Universidad de La Laguna, Calle Astrofísico Francisco Sánchez s/n, 38206 La Laguna, Tenerife, Spain
[13] School of Physics and Astronomy, Sun Yat-sen University, Zhuhai Campus, 2 Daxue Road, Xiangzhou District, Zhuhai, PR China
[14] Department of Astrophysics, University of Vienna Türkenschanzstraße 17, 1180 Vienna, Austria

Received 9 April 2020 / Accepted 11 May 2020

ABSTRACT

Context. A possible pathway for understanding the events and the mechanisms involved in galaxy formation and evolution is an in-depth investigation of the galactic and inter-galactic fossil sub-structures with long dynamical timescales: stars in the field and in stellar clusters.
Aims. This paper continues the Fornax Deep Survey (FDS) series. Following previous studies dedicated to extended Fornax cluster members, we present the catalogs of compact stellar systems in the Fornax cluster, as well as extended background sources and point-like sources.
Methods. We derived *ugri* photometry of ∼1.7 million sources over the ∼21 square degree area of FDS centered on the bright central galaxy NGC 1399. For a wider area, of ∼27 square degrees extending in the direction of NGC 1316, we provided *gri* photometry for ∼3.1 million sources. To improve the morphological characterization of sources, we generated multi-band image stacks by coadding the best-seeing *gri*-band single exposures with a cut at full width at half maximum ($FWHM$) ≤ 0.″9. We used the multi-band stacks as master detection frames, with a FWHM improved by ∼15% and a FWHM variability from field to field reduced by a factor of ∼2.5 compared to the pass-band with the best FWHM, namely the *r*-band. The identification of compact sources, in particular, globular clusters (GC), was obtained from a combination of photometric (e.g., colors, magnitudes) and morphometric (e.g., concentration index, elongation, effective radius) selection criteria, also taking as reference the properties of sources with well-defined classifications from spectroscopic or high-resolution imaging data.
Results. Using the FDS catalogs, we present a preliminary analysis of GC distributions in the Fornax area. The study confirms and extends further previous results that were limited to a smaller survey area. We observed the inter-galactic population of GCs, a population of mainly blue GCs centered on NGC 1399, extending over ∼0.9 Mpc, with an ellipticity $\epsilon \sim 0.65$ and a small tilt in the direction of NGC 1336. Several sub-structures extend over ∼0.5 Mpc along various directions. Two of these structures do not cross any bright galaxy; one of them appears to be connected to NGC 1404, a bright galaxy close to the cluster core and particularly poor in GCs. Using the *gri* catalogs, we analyze the GC distribution over the extended FDS area and do not find any obvious GC sub-structure bridging the two brightest cluster galaxies, namely, NGC 1316 and NGC 1399. Although NGC 1316 is more than twice as bright of NGC 1399 in optical bands, using *gri* data, we estimate a GC population that is richer by a factor of ∼3–4 around NGC 1399, as compared to NGC 1316, out to galactocentric distances of ∼40′ or ∼230 kpc.

Key words. galaxies: elliptical and lenticular, cD – galaxies: individual: NGC 1399 – galaxies: individual: NGC 1316 – galaxies: clusters: individual: Fornax – galaxies: evolution – galaxies: stellar content

* Full Tables 3–6 are only available at the CDS via anonymous ftp to cdsarc.u-strasbg.fr (130.79.128.5) or via http://cdsarc.u-strasbg.fr/viz-bin/cat/J/A+A/639/A136

1. Introduction

The study of local complexes of galaxies – galaxy clusters and groups– is crucial for attaining an understanding of the history of formation and evolution of the Universe through its building blocks. Local galaxy systems mark the endpoint of the evolution of galaxies after billion years of interactions, of varying intensities, with their companions (e.g., Mo et al. 2010).

A detailed study of the two extreme structures in terms of stellar density offers precious information on the history of formation and interactions of a galaxy: faint extended stellar features in the outskirts of galaxies, characterized by low star density and very long dynamical mixing timescales (Johnston et al. 2008), along with compact stellar systems, which are intrinsically bright, have typically old ages and have orbits that can trace recent and ancient accretion events (Brodie & Strader 2006). The stratification of dense star clusters and low surface brightness features can aid in probing a galaxy environment on different timescales from the earliest epoch of formation to the most recent merging events (e.g., West et al. 2004; Bournaud & Bournaud 2011).

In the last decade, also thanks to the advent of efficient large-format imaging cameras, a number of observational programs have carried out intensive surveys dedicated to covering large sections of nearby galaxy systems, superseding, in terms of both limiting magnitude and spatial resolution, any previous optical or near-IR study (e.g., Ferrarese et al. 2012; Iodice et al. 2016), thus providing a rich variety of data ideal for investigating compact stellar systems and faint stellar structures in different galaxy environments (de Jong et al. 2013; Muñoz et al. 2014; Durrell et al. 2014; Iodice et al. 2019; Venhola et al. 2019; Wittmann et al. 2019)

Within this framework, the Fornax Deep Survey (FDS) has carried out observations of the Fornax galaxy cluster centered on NGC 1399 out to one virial radius and further extended observations in the direction of the Fornax A sub-cluster in the South-West with its brightest member, NGC 1316, with a list of scientific topics: diffuse light and intracluster medium (Iodice et al. 2016), galaxy scaling relations (Iodice et al. 2019; Venhola et al. 2017, 2019; Raj et al. 2019), extragalactic star clusters and, more generally, compact stellar systems (D'Abrusco et al. 2016; Cantiello et al. 2018a), etc. In addition, the survey also contributes to research programs dealing with the study of the background galaxy population (e.g., identification of lensed systems and of their physical properties) and spectroscopic programs – for globular clusters (Pota et al. 2018), planetary nebulae (Spiniello et al. 2018), IFU study of galaxies in the cluster (Mentz et al. 2016).

The aim of this paper is to present the photometric and morphometric catalog of all point-like and slightly extended sources of the survey, along with a description of the methodology used to characterize the sources. As key topics of the survey, we present a preliminary study of compact stellar systems, including globular clusters (GCs) and ultra compact dwarf galaxies (UCDs).

Extragalactic, unresolved GCs are possibly the simplest class of astrophysical objects beyond stars. To a first approximation, GCs host a simple (that is single age and single metallicity) stellar population. In spite of the results on multiple populations in globular clusters (e.g., Piotto et al. 2007; Carretta et al. 2009; Bastian & Lardo 2018), it is doubtless that GCs host a stellar population that is much simpler than galaxies, in terms of the metallicity and age distributions, because their simpler star-formation history makes it possible to constrain the properties of these systems at a higher level of precision with regard to more complex and massive stellar systems.

The intrinsic simplicity of GCs, and of similar compact stellar systems, together with the old ages and the high luminosity, make these astronomical sources powerful and robust tracers of a galaxy and its environment, suitable to study a galaxy and its relevant structures out to cosmological distances (Alamo-Martínez et al. 2013; Janssens et al. 2017; Vanzella et al. 2017). The rich set of observables of stellar clusters makes them useful fossil records of the history of the evolution of their host galaxy and indicators of some of its physical property (distance, merging history, mass, metallicity, etc.). Here we focus on preliminary projected distribution maps of GCs and UCDs, and postpone further analysis of these sources to a forthcoming paper (Cantiello et al., in prep.).

In the following sections, we assume a distance modulus of $(m-M) = 31.51 \pm 0.03\,(\mathrm{ran.}) \pm 0.15\,(\mathrm{sys.})$ mag for the Fornax galaxy cluster, corresponding to $d = 20.0 \pm 0.3$ (ran.) $\pm$ 1.4 (sys.) Mpc (Blakeslee et al. 2009).

The paper is organized as follows. In Sect. 2, we describe the data, the procedures for source identification, calibration, and characterization, and we present the final FDS catalog of compact and slightly extended sources, as well as background galaxies. Section 3 is dedicated to a pilot application of the catalogs aimed at deriving 2D distributions of compact sources in the area. In Sect. 4, we report on the application to a science case for background sources. A brief summary of our conclusions is presented in Sect. 5.

2. Data and data analysis

2.1. Observations and data reduction

The observations used in this work are part of the now-completed FDS survey. The FDS consists of a combination of guaranteed time observations from the Fornax Cluster Ultra-deep Survey (FOCUS, P.I. R. Peletier) and the VST Early-type GAlaxy Survey (VEGAS, P.I. E. Iodice). The surveys were both performed with the ESO VLT Survey Telescope (VST), which is a 2.6 m diameter optical survey telescope located at Cerro Paranal, Chile (Schipani et al. 2010). The imaging is in the u, g,r and i-bands using the 1×1 square degree field of view camera OmegaCAM (Kuijken 2011).

The main body of the FDS dataset is centered on NGC 1399, the second brightest galaxy of the Fornax galaxy cluster in optical bands and the brightest galaxy of the main cluster. It consists of 21 VST fields with a complete *ugri* coverage. Further five fields in the *gri* bands extend in the south-west direction of the cluster, the Fornax A sub-cluster which covers the regions of the brightest cluster galaxy, the peculiar elliptical NGC 1316. For sake of clarity, in the following, we refer to the 21 FDS fields with *ugri* as FDS survey, and to the entire sample of 26 fields with *gri* coverage as FDS-extended, or FDSex. The FDS and FDSex areas are shown in Fig. 1; some of the known objects available from the literature and from previous FDS works are marked in the left panel of the figure.

The data, data acquisition, and reduction procedures have been presented in a number of papers of the FDS series (Iodice et al. 2016, 2017a,b, 2019; Venhola et al. 2017, 2018, 2019). A full description of the observations and the pipeline used for data reduction (AstroWISE; McFarland et al. 2013) steps are given in the cited papers, and in Peletier et al. (in prep.). In the following, we describe two critical differences with respect to previous works, specifically related to the focus on compact stellar systems in the present work.

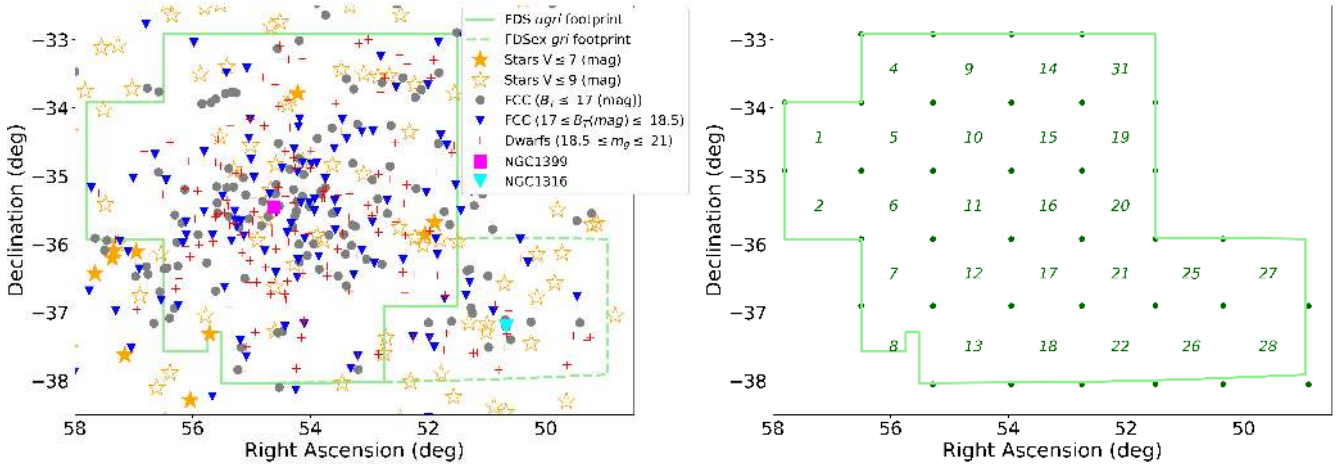

Fig. 1. *Left panel*: FDS footprint of the area covered by *ugri* photometry (green solid line), and by only *gri* (dashed green line). Other sources from catalogs available in the literature are also shown, as labeled. Bright galaxies from the Fornax Cluster Catalog (Ferguson 1989) are subdivided into two categories: likely members brighter than $B_T = 17$ mag and with $17 \leq B_T$ (mag) ≤ 18.5 (filled gray circles and blue triangles, respectively; from Ferguson 1989, Table II). Dwarf galaxies from FDS by Venhola et al. (2018), in the magnitude range $18.5 \leq m_g$ (mag) ≤ 21, are indicated with red crosses. The positions of the two brightest galaxies, NGC 1316 and NGC 1399, are also shown with a filled cyan triangle and a magenta square, respectively. Orange filled or empty five-pointed stars mark those stars with $m_V \leq 7/ \leq 9$ mag, respectively. *Right panel*: FDS and FDSex area. Green lines mark the edges of the survey, green bullets show the edges of single pointings; the ID of the field is also indicated.

2.2. Multi-band image stacks

The FDS standard reduction pipeline produced imaging data for many different scientific cases, with a general focus on extended galaxies in the cluster (e.g., Spavone et al. 2017). In Cols. (2–5) of Table 1, we report the median full width at half maximum (FWHM) of the point spread function (PSF) in arcseconds for each FDS VST field and for each available band; the FWHM distributions are also shown in the histograms of Fig. 2. The large FWHM variation, up to ∼50% for different fields observed in the same passband, may represent a limitation to the effectiveness of the FDS dataset for the science cases related to compact objects (foreground MW stars, background galaxies, GCs host in Fornax, etc.). The typical FWHM scatter of the exposures combined to obtain the single FDS fields stacks is $\mathrm{rms_{MAD}} = 0\farcs36,\ 0\farcs21,\ 0\farcs33,\ 0\farcs21$ in $u/g/r/i$-band, respectively[1].

To improve the detection and characterization of compact sources, we combined in a single coadded image all single VST exposures in g, r and i bands with a median FWHM lower than a fixed upper limit, u-band exposures were ignored because of the lower signal-to-noise and worse FWHM. After various experiments, we fixed the FWHM limit to $0\farcs9$: if a lower FWHM cut is adopted, the final resolution of the stack improves, at the expenses of a worse detection limit and larger field-to-field mean FWHM variability; a higher FWHM cut, instead, would make ineffective the use of multi-band stacks compared to single bands images. Hence, the $0\farcs9$ cut is adopted as the trade off between needs of better resolution and uniformity of the master detection frame. The combined image was processed as the single band images, except for the photometric calibration which is not derived. In the following, we refer to the coadd of *gri* exposures with FWHM cut as a-stack, and use the subscript a to identify the quantities derived from it. With this procedure, a new frame with narrower and more stable FWHM compared with *ugri* bands is obtained, and used as master detection frame. This improved both the uniformity of detections over the different FDS fields, and the determination of the morphological properties of the sources, allowing more accurate characterization of compact and point-like objects. These a-stacks will not be used to define absolute quantities (like calibrated magnitudes), but only for relative ones (like the CI_n, see below), thus the wavelength dependence of the PSF and source morphology will not be an issue.

As shown in Table 1, the a-stacks have a median FWHM smaller by ∼15% and with an rms scatter a factor of ∼2.5 lower than the median and rms of the FWHM for the best passband, namely the r-band. In Fig. 3 we show a $1' \times 1'$ thumbnail of the same FDS region in g, r, and i-band and the a-stack image centered on background spiral galaxy in the field FDS#5 (FCCB 1532, Ferguson 1989). In general, the depth of the coadded multiband a-stack does not change much compared with the best band of the field, because the reduced number of exposures used is compensated by the better S/N due to the higher spatial resolution. The spatial resolution, however, is in all cases enhanced, as shown in the $FWHM_a$ column in Table 1.

2.3. Photometry and photometric calibration

Catalogs were derived for each single FDS pointing; the identification of fields with available data is shown in the right panel of Fig. 1. To increase the contrast of faint sources close to the cores of extended galaxies, before running the procedures to obtain the photometry and the morphometry (like FWHM, elongation, flux radius, etc.; see Sect. 2.4 below) we modeled and subtracted all Fornax members brighter than $B_T \sim 18$ mag. The fit of the isophotes is performed using the IRAF STSDAS task ELLIPSE, which is based on an algorithm by Jedrzejewski (1987).

To obtain the photometry of sources in FDS frames, we used a combination of procedures, based on SExtractor (Bertin & Arnouts 1996) and DAOphot (Stetson 1987) runs, and

[1] The median absolute deviation, MAD, defined as $\mathrm{MAD} = \mathrm{median}|X_i - \mathrm{median}(X)|$, is a robust indicator of the rms, which cleans the rms from the spurious presence of few outliers in the sample. For a Gaussian distribution the standard deviation is $\mathrm{rms} \sim 1.48 \times \mathrm{MAD}$.

Table 1. Image quality parameters for FDS and FDSex fields.

Field ID	$FWHM_u$ ($''$)	$FWHM_g$ ($''$)	$FWHM_r$ ($''$)	$FWMH_i$ ($''$)	$FWHM_a$ ($''$)	$\langle P_2(s)\rangle$ (mag)	$\sigma[P_2(s)]$ (mag)	$\langle P_2(w)\rangle$ (mag)	$\sigma[P_2(w)]$ (mag)	$\langle P_2(x)\rangle$ (mag)	$\sigma[P_2(x)]$ (mag)	$u_{\rm lim}$ (mag)	$g_{\rm lim}$ (mag)	$r_{\rm lim}$ (mag)	$i_{\rm lim}$ (mag)
(1)	(2)	(3)	(4)	(5)	(6)	(7)	(8)	(9)	(10)	(11)	(12)	(13)	(14)	(14)	(16)
1	1.17 ± 0.03	1.35 ± 0.12	1.14 ± 0.11	0.69 ± 0.08	0.72 ± 0.08	0.006	0.019	0.018	0.024	0.014	0.030	24.24 ± 0.13	25.39 ± 0.10	24.65 ± 0.17	24.53 ± 0.15
2	1.21 ± 0.08	1.11 ± 0.16	0.89 ± 0.05	0.79 ± 0.09	0.79 ± 0.04	0.008	0.018	0.011	0.020	0.005	0.032	24.02 ± 0.18	25.41 ± 0.13	25.04 ± 0.12	24.12 ± 0.13
4	1.19 ± 0.05	1.39 ± 0.13	1.19 ± 0.09	0.70 ± 0.07	0.71 ± 0.07	0.007	0.020	0.052	0.026	−0.005	0.029	24.12 ± 0.09	25.35 ± 0.10	24.65 ± 0.11	24.44 ± 0.14
5	1.35 ± 0.07	1.17 ± 0.14	0.98 ± 0.06	1.11 ± 0.16	0.82 ± 0.09	0.005	0.018	0.007	0.024	0.012	0.033	24.05 ± 0.17	25.48 ± 0.10	24.72 ± 0.08	23.88 ± 0.10
6	1.13 ± 0.07	0.83 ± 0.04	1.08 ± 0.12	1.24 ± 0.14	0.80 ± 0.05	0.005	0.021	0.023	0.023	−0.007	0.033	24.22 ± 0.10	25.70 ± 0.10	24.66 ± 0.14	23.51 ± 0.09
7	1.03 ± 0.06	0.82 ± 0.04	0.90 ± 0.07	1.44 ± 0.13	0.78 ± 0.08	0.007	0.022	0.012	0.020	0.008	0.026	24.16 ± 0.12	25.79 ± 0.11	24.91 ± 0.13	23.35 ± 0.11
8	1.21 ± 0.10	0.93 ± 0.16	0.90 ± 0.12	0.96 ± 0.18	0.84 ± 0.13	0.006	0.021	0.022	0.024	−0.015	0.033	24.23 ± 0.21	25.50 ± 0.22	24.99 ± 0.21	23.72 ± 0.20
9	1.42 ± 0.08	1.20 ± 0.07	0.97 ± 0.08	0.84 ± 0.07	0.82 ± 0.05	0.003	0.022	0.036	0.021	−0.015	0.035	23.96 ± 0.09	25.50 ± 0.12	25.06 ± 0.13	24.38 ± 0.13
10	1.34 ± 0.06	1.15 ± 0.05	0.96 ± 0.07	1.09 ± 0.11	0.86 ± 0.05	0.000	0.018	0.009	0.014	−0.010	0.026	24.09 ± 0.10	25.52 ± 0.09	24.84 ± 0.11	23.96 ± 0.11
11	1.27 ± 0.06	1.09 ± 0.14	1.08 ± 0.14	1.17 ± 0.10	0.84 ± 0.08	0.011	0.023	0.025	0.024	−0.002	0.032	24.09 ± 0.13	25.22 ± 0.10	24.65 ± 0.11	23.64 ± 0.09
12	1.18 ± 0.08	0.80 ± 0.04	0.97 ± 0.07	1.17 ± 0.09	0.80 ± 0.05	0.014	0.024	0.022	0.021	0.001	0.037	24.30 ± 0.09	25.74 ± 0.11	24.85 ± 0.11	23.61 ± 0.09
13	1.10 ± 0.05	0.91 ± 0.05	1.03 ± 0.08	1.16 ± 0.07	0.89 ± 0.05	0.003	0.016	0.021	0.016	−0.003	0.029	24.39 ± 0.18	25.72 ± 0.13	24.99 ± 0.12	24.22 ± 0.13
14	1.46 ± 0.09	1.18 ± 0.09	0.96 ± 0.08	0.85 ± 0.06	0.83 ± 0.06	0.004	0.019	0.012	0.017	0.005	0.028	23.99 ± 0.08	25.43 ± 0.12	24.94 ± 0.13	24.30 ± 0.12
15	1.30 ± 0.05	1.13 ± 0.04	0.88 ± 0.04	0.98 ± 0.09	0.81 ± 0.06	0.001	0.020	0.008	0.022	−0.001	0.031	24.19 ± 0.11	25.37 ± 0.09	25.10 ± 0.08	24.02 ± 0.16
16	1.31 ± 0.04	1.26 ± 0.08	0.91 ± 0.08	1.09 ± 0.07	0.84 ± 0.05	0.008	0.025	0.006	0.020	−0.000	0.035	24.16 ± 0.11	25.31 ± 0.08	24.93 ± 0.11	23.88 ± 0.09
17	1.27 ± 0.06	1.25 ± 0.16	0.82 ± 0.05	1.01 ± 0.07	0.80 ± 0.04	−0.006	0.020	0.020	0.020	−0.011	0.032	24.17 ± 0.09	25.16 ± 0.18	25.21 ± 0.11	24.01 ± 0.10
18	1.12 ± 0.08	0.94 ± 0.05	1.03 ± 0.07	1.12 ± 0.12	0.87 ± 0.09	−0.002	0.018	0.021	0.016	0.007	0.025	24.19 ± 0.23	25.57 ± 0.13	24.93 ± 0.12	24.14 ± 0.13
19	1.26 ± 0.05	1.14 ± 0.09	0.89 ± 0.05	0.86 ± 0.06	0.79 ± 0.05	0.010	0.022	0.042	0.022	0.009	0.025	24.10 ± 0.11	25.46 ± 0.09	25.15 ± 0.10	24.13 ± 0.13
20	1.30 ± 0.05	1.23 ± 0.06	0.92 ± 0.09	1.08 ± 0.08	0.81 ± 0.08	0.019	0.033	−0.006	0.032	0.002	0.044	24.12 ± 0.11	25.17 ± 0.12	24.76 ± 0.13	23.80 ± 0.12
21	1.22 ± 0.05	1.12 ± 0.06	0.78 ± 0.05	0.88 ± 0.08	0.78 ± 0.04	0.001	0.022	0.004	0.027	0.002	0.035	24.06 ± 0.11	25.22 ± 0.09	24.92 ± 0.12	24.22 ± 0.09
22	…	1.03 ± 0.06	0.80 ± 0.06	0.85 ± 0.05	0.79 ± 0.05	…	…	0.004	0.019	0.007	0.029	…	25.27 ± 0.14	24.92 ± 0.13	24.21 ± 0.10
25	…	1.12 ± 0.05	0.76 ± 0.06	0.85 ± 0.08	0.78 ± 0.08	…	…	0.016	0.025	−0.003	0.031	…	25.36 ± 0.11	24.98 ± 0.12	24.10 ± 0.10
26	…	0.95 ± 0.12	0.80 ± 0.04	0.91 ± 0.08	0.78 ± 0.04	…	…	0.037	0.021	−0.018	0.035	…	24.79 ± 0.15	25.00 ± 0.11	23.94 ± 0.13
27	…	1.05 ± 0.09	0.78 ± 0.06	0.89 ± 0.09	0.77 ± 0.08	…	…	0.012	0.026	−0.007	0.042	…	25.19 ± 0.11	24.79 ± 0.15	23.75 ± 0.16
28	…	1.09 ± 0.07	0.79 ± 0.15	0.91 ± 0.11	0.78 ± 0.10	…	…	0.007	0.035	0.013	0.032	…	25.11 ± 0.13	24.65 ± 0.19	23.78 ± 0.14
31	1.46 ± 0.08	1.22 ± 0.06	1.00 ± 0.07	0.86 ± 0.08	0.84 ± 0.05	0.012	0.022	0.030	0.023	0.003	0.032	23.83 ± 0.11	25.31 ± 0.11	24.78 ± 0.15	24.05 ± 0.17
Median	1.26 ± 0.11	1.12 ± 0.15	0.92 ± 0.11	0.94 ± 0.17	0.80 ± 0.04	0.006	0.021	0.017	0.022	0.000	0.032	24.12 ± 0.13	25.38 ± 0.17	24.92 ±0.17	24.02 ± 0.24

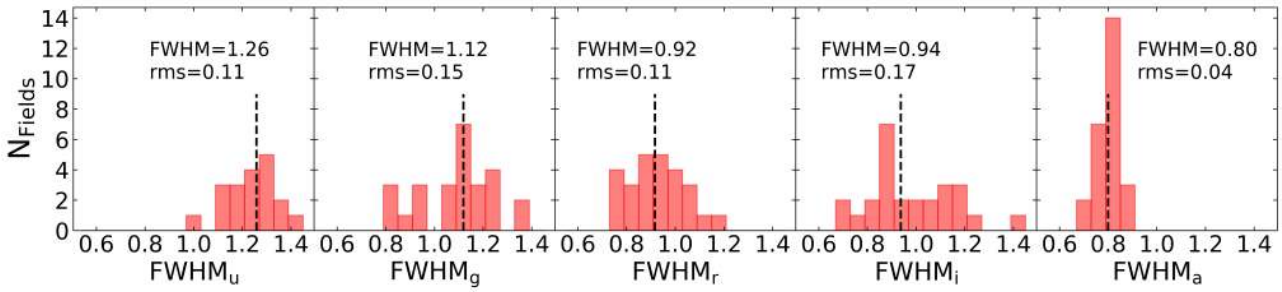

Fig. 2. Histograms of the median PSF FWHM of the FDS fields in the four available passbands, plus the multi-band *a*-stacks. The vertical dashed line shows the median of the ensemble.

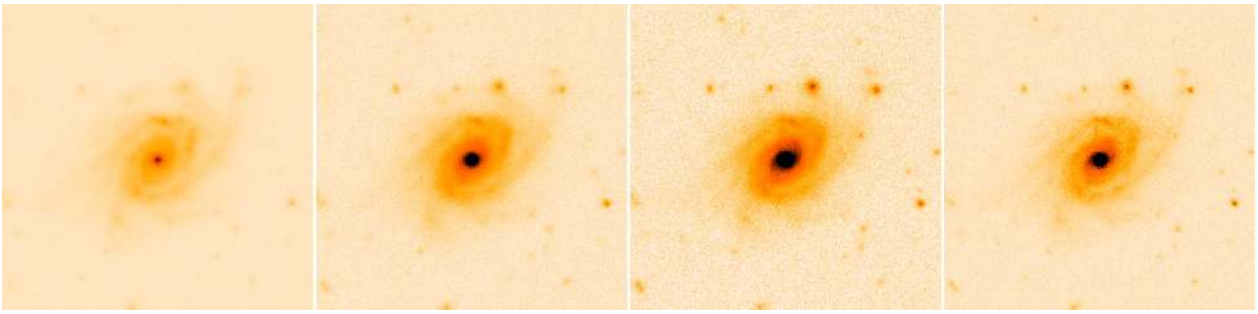

Fig. 3. *From left to right*: *g*, *r*, *i*-band and *a*-stack of a background spiral galaxy in the field FDS#5 (FCCB 1532, Ferguson 1989). *Rightmost panel*: derived from the combination of the sub-exposures of the *first three panels*, selecting only the ones with lowest atmospheric turbulence (see text).

codes developed by the first author. We adopt AB mag photometric system, as in previous FDS works. The galaxy-subtracted frames used in this stage are already calibrated as described in the previous works of the FDS series (see below).

First, we used SExtractor to obtain the mean properties of each frame, like the FWHM; the reference morphometry for each source is obtained from the *a*-stacks, though we also derived the morphometric properties for all available passbands. Then, DAOphot is run on the *a*-stacks, and fed to our procedure to identify bright, non-saturated and isolated stars needed to obtain a variable PSF model over the single pointing. Typically, with this procedure we selected ∼200 candidate PSFs per single FDS field, that were visually inspected in all bands to remove candidates contaminated by faint companions, bright halos of

Table 2. FDS magnitudes compared with APASS and SM.

Filter	$\mathrm{rms}_{\mathrm{VST-APASS}}$	$\Delta\mathrm{mag}_{\mathrm{FDS-SM}}$	$\mathrm{rms}_{\mathrm{VST-SM}}$
u	0.13	−0.054	0.066
g	0.03	0.149	0.031
r	0.05	−0.015	0.028
i	0.07	−0.003	0.025

galaxies or saturated stars, or other instrumental artifacts. Using this iterative process, we ended up with a typical list of 50 to 100 point-like sources to model the PSF with DAOphot for each filter and field. The list of PSFs was then fed to DAOphot for PSF modeling, adopting the variable PSF option. The first complete DAOphot run was on the *a*-stack. The output table for this run was used to (*i*) identify sources to define a master detection catalog, (*ii*) obtain the DAOphot sharpness parameter that would then be used as additional parameter for selecting good candidate compact sources.

The master detection catalog was then given as input to run DAOphot on each available filter and for all fields: *ugri* for the FDS area, *gri* for FDSex. We also run SExtractor on the full set of images, to obtain the aperture magnitude within 8-pixel diameter (MAG_APER) and the automated aperture magnitude derived from Kron (1980) for first moment algorithms (MAG_AUTO), with the respective photometric errors[2]. For the aperture magnitudes, after some tests we adopted the eight-pixel diameter: larger diameters implied larger statistical errors on derived magnitudes (because of the noisier background and higher contamination from neighboring sources), smaller diameters suffered from larger systematic errors (because larger aperture corrections are needed). Both MAG_APER(8) and MAG_AUTO are stored in our final catalogs. It is, in particular, MAG_AUTO that provides a good choice for the magnitude of non-compact background objects.

The photometric calibration is carried out in two steps. The first is the same described in Venhola et al. (2018) and uses standard star fields observed each night and comparing their OmegaCAM magnitudes with the final data from the Sloan Digital Sky Survey Data III (Alam et al. 2015).

With such calibration, and after applying the field and passband dependent aperture corrections, the photometry of the same sources in different adjacent FDS pointings shows a spatially variable offset, with a median upper limit of ∼0.1 mag. This might be a consequence of the different (mean) photometric conditions for neighboring FDS fields during the FDS observing runs which span a time interval of ∼5 years.

As a second step of the photometric calibration, to improve the photometric uniformity and consistency over the FDS (and FDSex) area, and to derive the spatially and filter dependent aperture correction map, we compared our VST photometry of bright non-saturated point-like sources to the APASS photometry[3] and obtained the two-dimensional map that best matches the two datasets. The map is derived for each field separately, using a support vector machine (SVM) supervised learning method, with a radial basis function (RBF) kernel (Pedregosa et al. 2011). Only isolated unsaturated stars, brighter than a given magnitude cut (19/17/17/16.5 mag in $u/g/r/i$ band, respectively), are used in the regression algorithm.

The correction maps are derived from 200 to 300 stars per FDS field, the final median $\mathrm{rms}_{\mathrm{VST-APASS}}$ between VST and APASS photometry over the full set of re-calibrated frames is reported in Table 2. Figure 4 shows an example of the correction maps derived for the field FDS#19. Each correction map is then applied to its specific field and passband, to correct the photometry of all sources detected in the specific FDS pointing.

Because APASS lacks u coverage, for such passband we adopted a slightly different re-calibration strategy. After the preliminary calibration described above, the B-band magnitudes of stars from APASS were transformed to u-band using Lupton (2005) transformation equations available from the SDSS web pages[4]. In particular: $u = B_{\mathrm{APASS}} + 0.8116 \cdot (u-g)_{\mathrm{fit}} - 0.1313$, where the $(u-g)_{\mathrm{fit}}$ color index is derived from the APASS $(g-i)$ and $(g-r)$ indices, using a second degree polynomial fit derived from SDSS data over different sky regions[5]. From this stage on, by using the u-band magnitudes of stars in APASS derived as a function of the B, g, r, and i photometry, we may proceed to derive and apply the u-band correction maps as in *gri* bands.

To further verify the validity of the calibration obtained with the strategy delineated above, especially for the more elaborate u-band, we matched and compared our photometry to the SkyMapper (SM) data (Wolf et al. 2018; Onken et al. 2019). The SDSS photometric systems of APASS and SM are not equivalent, the u and g bands, in particular, show differences of up to 0.5 mag in the two systems (Wolf et al. 2018). However, within the color interval $|g-i| \leq 1$ mag, the SM to SDSS difference for *uri*-bands is $\lesssim 0.1$ mag, while it is a factor of ∼4 larger in g-band (Wolf et al. 2018, see their Fig. 17 and Sects. 2.2, 5.4). Hence, as a further consistency check, we compare our VST re-calibrated photometry to SM data, within the color interval $|g-i| \leq 1$ mag.

Over the entire FDS area covered with *ugri* observations, we found ∼46 500 sources in common with SM. After identifying bright and isolated stars, and with the given prescriptions on $(g-i)$ color selection, the final sample contains ∼4600 objects (∼220 per FDS field).

Table 2 reports the median magnitude offsets between the FDS and SM photometry for the matched sources, together with the $\mathrm{rms}_{\mathrm{MAD}}$. With the only not unexpected exception of the g band we find good agreement between the u, r and i photometry, with magnitude offsets better than 0.02 mag in r and i bands and of ∼0.05 mag in u; the $\mathrm{rms}_{\mathrm{MAD}}$ is ∼0.03 in *gri* and about twice larger in u-band.

For an independent check of the g-band photometry, we used the data from the HST/ACS Fornax Cluster Survey (ACSFCS; Jordán et al. 2007, 2015). In Fig. 5, we report a comparison of our and ACSFCS g-band magnitudes. We matched the ∼6.300 GC candidates from the ACSFCS with the FDSex *gri* catalog, to avoid the worse completeness limit of the u-band in the *ugri* catalogs. Adopting a matching radius of 1.″0, a total of 3750 sources are found in common to both catalogs. The completeness of the matching is ∼90% or higher at bright magnitudes ($m_g \leq 23$), decreases to ∼80% for $m_g \leq 24$, and is lower than ∼70% for $m_g \leq 25$. Hence, the completeness of the *gri* catalog drops quickly below $m_g \sim 24.5$ (mag), which corresponds to ∼0.5 mag fainter than the turn over magnitude (TOM) of the GC luminosity function (GCLF) for galaxies in Fornax (Villegas et al. 2010).

[2] For SExtractor runs, we adopted Gaussian convolution kernels of different sizes depending on the FWHM of the field.

[3] Visit the URL `https://www.aavso.org/`

[4] `http://www.sdss3.org/dr8/algorithms/sdssUBVRITransform.php`, Lupton (2005).

[5] The fitted relation is: $(u-g)_{\mathrm{fit}} = P_{00} + (g-i)_{\mathrm{APASS}} \times P_{10} + (g-r)_{\mathrm{APASS}} \times P_{01} + (g-i)^2_{\mathrm{APASS}} \times P_{20} + (g-i)_{\mathrm{APASS}} \times (g-r)_{\mathrm{APASS}} \times P_{11} + (g-r)^2_{\mathrm{APASS}} \times P_{02}$, with $P_{00} = 0.1997$, $P_{10} = -0.1799$, $P_{01} = 2.849$, $P_{20} = 1.043$, $P_{11} = -3.498$, $P_{02} = 2.306$.

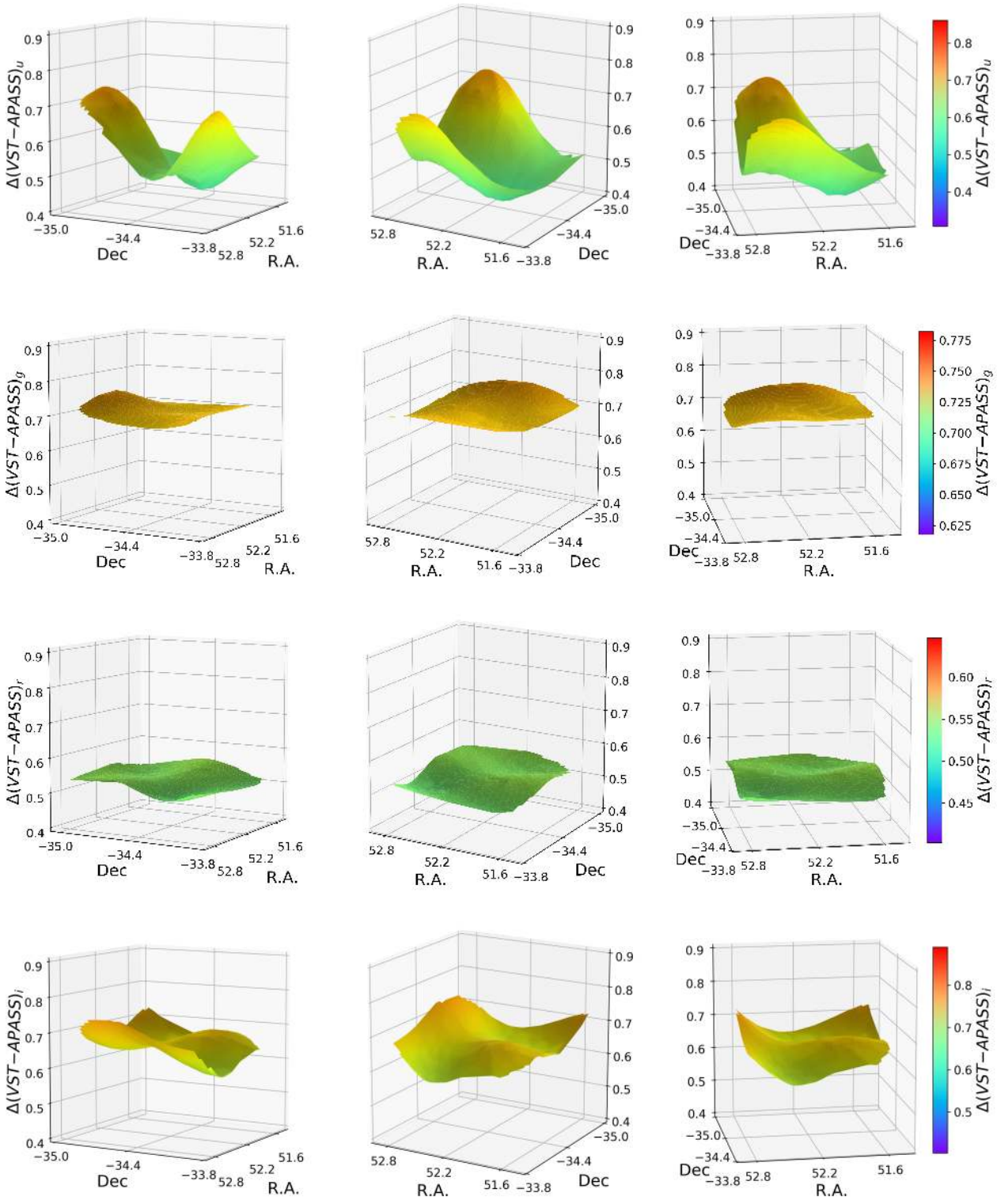

Fig. 4. Example of the two-dimensional photometric correction maps for refining the photometry of FDS fields. The maps also include the aperture correction term. Field FDS#19 is shown: u, g, r, and i-band correction maps are plotted *from upper to lower panels*, respectively. For each passband, the surface correction map is shown with the same color coding and for different viewpoints in each of the three panels.

The left panel of Fig. 5 shows the VST to ACSFCS g-band magnitude difference versus m_g (blue dots in the figure). From the matched catalog, we selected a reference GC sample (see next section), marked as red dots in the figure. The running mean difference for both the full matched sample and the reference sample are shown in the middle panel, adopting window bin size 100/50 for the full/best sample, respectively. Finally, the right panel of the diagram shows the same quantities as in the left one, but versus the $(g-i)$ color. In all cases shown, the difference is consistent with zero – Δg(FDS−ACSFCS) = -0.03 ± 0.12 for

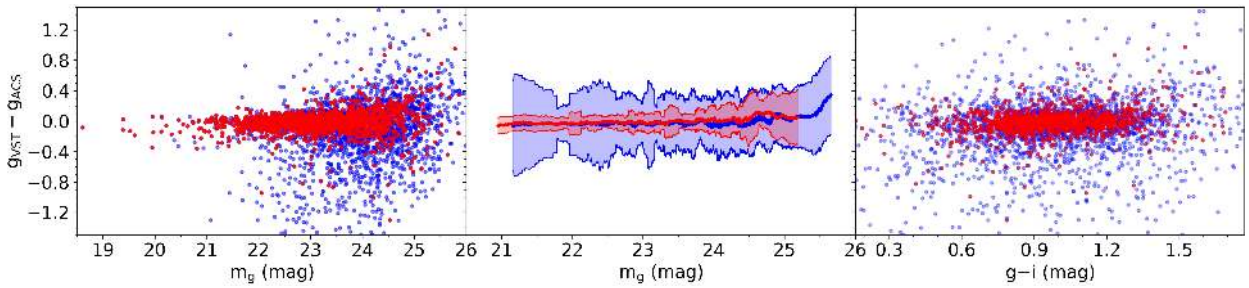

Fig. 5. *Left panel*: g-band magnitudes from FDS compared with magnitudes of GC candidates from the ACSFCS. Blue symbols show the full matched set, red symbols identify compact sources in our reference catalog (see text). *Middle panel*: as left panel, but running averages are shown, with bin size of 100/50 objects for the blue/red symbols, respectively. *Right panel*: as left panel, but versus $(g-i)$ color.

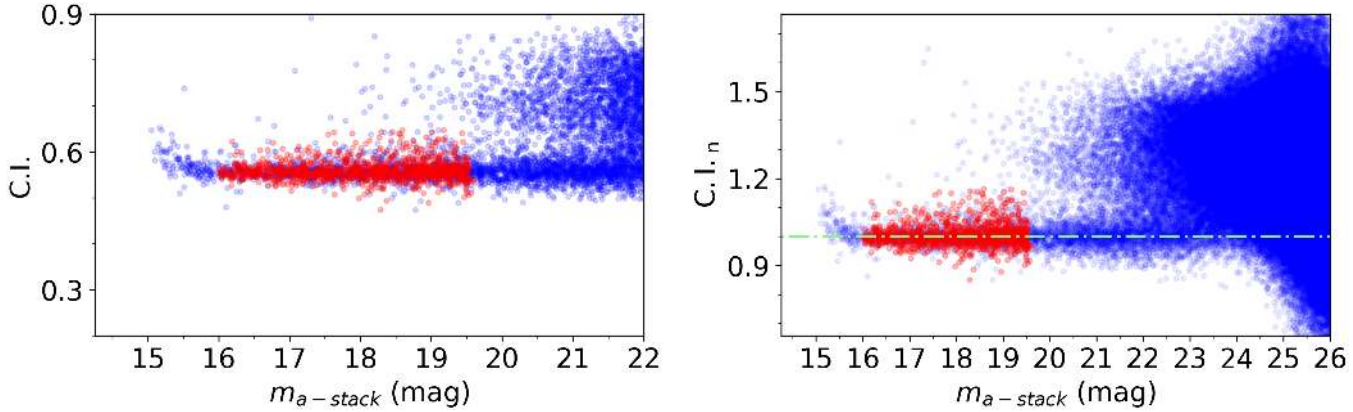

Fig. 6. Normalization procedure for the CI, data for the field FDS#13 are shown. *Left panel*: concentration index $CI = \mathrm{mag}_{4\ \mathrm{pix}} - \mathrm{mag}_{6\,\mathrm{pix}}$ versus the uncalibrated a-stack magnitude. For the sake of clarity, only the brightest magnitude range is shown. Blue dots refer to the full sample, red symbols to candidate compact sources used to derive the median CI factor for normalization. *Right panel*: same as left panel, but over a larger magnitude range and after normalization to the median CI of bright point-like sources (red dots). Point-like sources candidates are aligned along the sequence parallel to the x-axis, around $CI_n \sim 1$ (green dot-dashed line).

the full sample of 3750 matched sources; Δg(FDS−ACSFCS) = -0.01 ± 0.07 for the 1455 sources in the reference catalog – with no evidence of significant residual trends.

2.4. Morphometry

As already anticipated in Sect. 2.2, by morphometry we mean the measurement of all characteristics related to the shape of the source, our reference frames for the morphological characterization of sources are the multi-band a-stacks derived from *gri* exposures with the best seeing. We placed a particular emphasis on deriving quantities useful for distinguishing between point-like and extended sources and identified a number of useful features: FWHM, CLASS_STAR, flux radius, and elongation (major-to-minor axis ratio) derived with SExtractor, as well as the sharpness parameter derived from DAOphot.

For each source detected, we also measured the magnitude concentration index, described in Peng et al. (2011), defined as the difference in magnitude measured at two different radial apertures. Following various tests, we adopted as a reference the concentration index derived from the a-stacks aperture magnitudes at four and six pixels, namely: $CI = \mathrm{mag}_{4\ \mathrm{pix}} - \mathrm{mag}_{6\,\mathrm{pix}}$. For point-like sources, after applying the aperture correction to the PSF magnitudes of isolated stars at both radii, CI should be statistically consistent with zero. The concentration index is constant for point-like objects, while extended sources have variable CI larger than zero.

Because the a is not a real photometric band and because of the field-to-field variations for simplicity, we decided to normalize the CI index to 1, rather than to zero[6]. The normalization was derived as follows: for each field, we first estimated the CI from the magnitude difference within the two chosen apertures (so no aperture correction is applied), then derived the median CI of candidate point-like isolated and bright sources. Finally, the CI of the full sample was normalized to the median CI such that compact sources should, by construction, be characterized by normalized CI values, CI_n, of ∼1. Figure 6 shows the procedure described, for sources in the field FDS#13: as expected, compact sources (selected here using the morphological parameters from SExtractor) occupy a flat sequence of constant CI (left panel), normalized to one in the right panel of the figure.

2.5. Final catalog and data quality

The DAOphot and SExtractor catalogs of sources in the FDS fields can then be combined in one single catalog (the same is done, independently, for the FDSex regions). The final catalog contains: (i) source identification adopting the IAU naming

[6] The normalization to zero is the expected CI value for point-like sources after the proper aperture correction is applied to all sources. In our case, because the a-stacks are not in a real passband, and each FDS pointing has a different composition of good seeing g, r and i single exposures, we chose to avoid the aperture corrected normalization to zero.

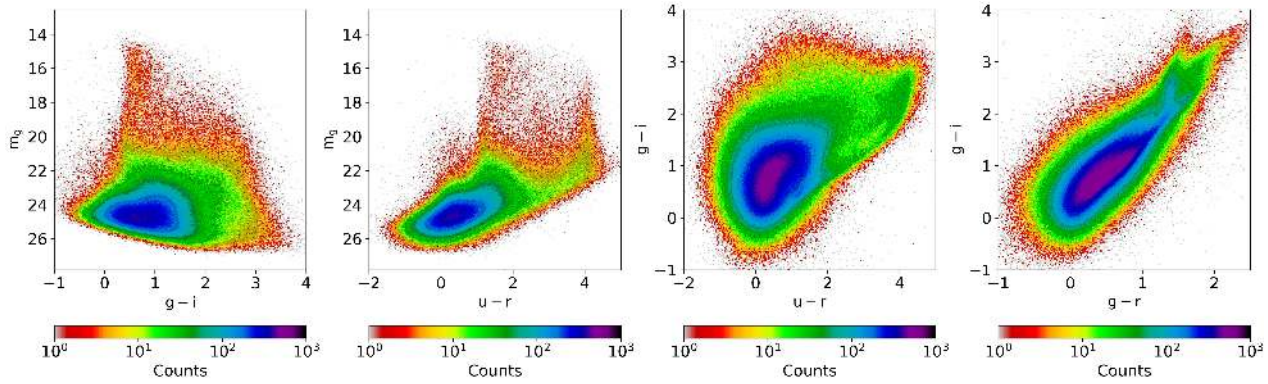

Fig. 7. Hess color–magnitude and color-color diagrams of the full sample with *ugri* photometry. Extinction corrected PSF magnitudes are used in all cases.

rules[7] and position from the *a*-stacks; (ii) the calibrated AB magnitudes from PSF photometry derived with DAOphot in all available bands; (iii) the uncorrected aperture and Kron-like magnitudes from SExtractor; (iv) the morphometric parameters for *a*-stacks (FWHM, CLASS_STAR, flux radius, elongation and sharpness), as well as the latter for all other available bands. The FDS catalog provides data based on the 21 FDS field in the *ugri*-bands, and for the *a*-stacks; a second *gri*-bands catalog for the full FDSex area is also generated.

In the catalogs, we include the extinction correction term, assuming the Galactic extinction values from the Schlafly & Finkbeiner (2011) recalibration of the Schlegel et al. (1998) infrared based dust maps. Figure 7 shows a selection of extinction corrected color magnitude and color-color diagrams for the full sample of sources in the FDS catalog.

As an overall photometric quality assessment, we used the principal colors, described in Ivezić et al. (2004). Principal colors are linear combinations of the SDSS colors of stars. We adopted the coefficients and selection parameters given in Tables 1–3 of Ivezić et al. (2004). The colors are combined to obtain a new color perpendicular to the stellar locus. Assuming the position of the locus to be fixed, the value of the principal colors is then an internal measure of the absolute photometric calibration of the data. Table 1 provides the median and rms width of three principal colors, $P2(s)$, $P2(w)$ and $P2(x)$ for each FDS field; the median P2 values over the full set of fields is <0.02 with rms $\lesssim$ 0.03. The $P_2(s)$ depends on the *u*-band photometry, and cannot be determined over the FDSex fields. The overall $\langle P_2 \rangle$ and $\sigma[P_2]$ values, and the values for each field, are consistent with the same value reported by Ivezić et al. (2004) for SDSS photometry.

Finally, we obtain the limiting magnitudes reported in Table 1 for all fields and bands, derived as 5σ magnitude integrated over the PSF, determined from the median S/N estimated as $\Delta m^{-1}_{\rm PSF}$. The median *g*-band limiting magnitude is $g_{\rm lim} \sim 25.4\pm 0.2$ mag; we note that the faintest GCs matched with the ACS-FCS reach $m_g \sim 25.6$ mag, which increases to $m_g \sim 25.2$ mag for the sources in the reference catalog.

All catalogs are available via a dedicated web-interface of the FDS team[8], and are made available through the CDS. An extract of the data for the ∼1.7 million *ugri* matched sources in the FDS catalog is reported in Table 3 (an extract for the ∼3.1 million sources in the FDSex *gri* catalog is given in Table 4).

[7] See https://www.iau.org/public/themes/naming/
[8] http://fdscat.oa-abruzzo.inaf.it/

3. A preliminary map of GCs and UCD galaxies over the FDS area

One of the goals of the FDS survey is to map the distribution of GCs and UCDs in Fornax out to the virial radius. In the following sections and, in further detail, in a forthcoming dedicated paper (Cantiello et al., in prep.), we analyze and discuss the cluster-wide properties of these two classes of compact stellar systems, with more emphasis on GCs.

Unambiguously identifying GCs from purely optical photometry is unfeasible. In Cantiello et al. (2018b) we showed that also spectroscopic samples might be affected by non negligible contamination. Muñoz et al. (2014) demonstrated that optical data including the *u* band, combined with *K*-band near-IR data can dramatically reduce the contamination by fore and background sources.

Lacking a publicly available deep near-IR survey covering the FDS area, we proceeded as previously in an earlier work on GCs from the VEGAS and FDS surveys (Cantiello et al. 2015, 2018a; Cantiello 2016; D'Abrusco et al. 2016). Briefly, we identify a master catalog of GCs, and UCDs, and use the main properties of confirmed sources to constrain the mean loci of several photometric (magnitudes, colors, etc.) and morphometric (CI_n, galaxy/star classification, etc.) indicators. In the following section we discuss the procedures adopted for identifying the loci of GCs using several parameters.

3.1. GCs and UCDs Master Catalogs

We define a master catalog of GCs and UCDs, taking as reference spectroscopic and photometric studies from the literature, adopting $M_g = -10.5$ mag as GC/UCD separation criteria, corresponding to $M_V \sim -11$ mag ($\sim 10^7\, M_\odot$), and to an apparent $m_g = 21$ magnitude at the adopted distance to Fornax (e.g., Mieske et al. 2004; Hilker et al. 2007). We collected photometric data from the previously mentioned ACSFCS survey (Jordán et al. 2007, 2015). The advantage of ACS with respect to other imagers is the very high resolution allowed by the space-based observations. At the distance of Fornax, GCs observed with the ACS camera appear as partially resolved sources, so their physical size can be estimated and used as a further parameter to reliably separate them from foreground stars and background galaxies. From the ACSFCS GC sample, we selected only GC candidates with a high probability $p_{\rm GC}$ of being a GC ($p_{\rm GC} \geq 0.75$, derived according to a maximum-likelihood estimate, Jordán et al. 2009).

Table 3. Extract of the FDS *ugri* catalog.

ID	RA (J2000)	Dec (J2000)	m_u	m_g	m_r	m_i	Star/Gal.	CI_n	F.R.	$FWHM$	Elong.	Sharp.	$E(B-V)$	Field
	(deg)	(deg)	(mag)	(mag)	(mag)	(mag)			(arcsec)	(arcsec)				(#)
(1)	(2)	(3)	(4)	(5)	(6)	(7)	(8)	(9)	(10)	(11)	(12)	(13)	(14)	(15)
FDSJ033744.66-345442.84	54.436077	−34.911900	21.550 ± 0.051	20.013 ± 0.053	19.172 ± 0.066	18.507 ± 0.059	0.029	1.449	2.51	2.77	1.260	4.559	0.011	10
FDSJ034014.64-345451.44	55.061020	−34.914288	21.675 ± 0.042	20.368 ± 0.039	19.509 ± 0.048	18.865 ± 0.037	0.029	1.266	1.47	2.49	1.670	3.240	0.012	10
FDSJ034028.79-345508.98	55.119957	−34.919163	18.585 ± 0.006	15.914 ± 0.005	14.790 ± 0.010	14.217 ± 0.006	0.996	1.040	0.65	0.91	1.010	0.872	0.012	10
FDSJ034055.30-345511.56	55.230427	−34.919880	24.431 ± 0.192	24.853 ± 0.124	24.014 ± 0.124	23.565 ± 0.154	0.830	1.243	0.69	1.60	1.570	0.920	0.011	10
FDSJ034044.55-345510.26	55.185608	−34.919518	25.478 ± 0.511	24.972 ± 0.116	24.841 ± 0.228	25.056 ± 0.507	0.512	1.304	0.45	0.69	1.700	1.218	0.011	10
FDSJ034036.60-345510.96	55.152508	−34.919712	24.901 ± 0.306	25.313 ± 0.171	25.395 ± 0.427	24.588 ± 0.348	0.562	0.659	0.33	0.40	1.340	−5.609	0.011	10
FDSJ034055.72-345510.38	55.232162	−34.919552	25.046 ± 0.358	24.225 ± 0.058	23.586 ± 0.074	22.863 ± 0.089	0.875	1.020	0.52	1.68	1.130	1.078	0.011	10
FDSJ034107.11-345506.88	55.279636	−34.918579	24.675 ± 0.284	25.149 ± 0.178	24.641 ± 0.258	24.698 ± 0.487	0.699	0.737	0.34	0.88	1.640	−6.010	0.011	10
FDSJ034015.36-345510.38	55.063984	−34.919552	25.319 ± 0.471	26.016 ± 0.316	24.720 ± 0.172	24.554 ± 0.457	0.430	1.082	0.42	0.76	1.200	−0.228	0.012	10
FDSJ033954.02-345511.46	54.975067	−34.919849	24.812 ± 0.326	24.716 ± 0.094	24.663 ± 0.168	23.768 ± 0.167	0.643	1.398	0.74	1.77	2.980	−1.337	0.012	10
FDSJ034037.01-345511.86	55.154224	−34.919960	24.901 ± 0.285	23.111 ± 0.026	22.269 ± 0.027	21.868 ± 0.038	0.980	0.956	0.54	0.91	1.080	−0.396	0.011	10
FDSJ033612.00-345454.11	54.050011	−34.915031	21.314 ± 0.059	20.323 ± 0.066	19.940 ± 0.081	19.444 ± 0.072	0.029	1.543	1.98	4.01	1.240	5.941	0.013	10

Notes. Columns list: (1) FDS ID; (2) Right Ascension; (3) Declination; (4-7) *ugri*-band magnitude with error; (8) Star/Galaxy classifier, CLASS_STAR, from SExtractor; (9) normalized concentration index; (10) Flux Radius, from SExtractor in arcseconds; (11) FWHM in arcseconds; (12) Elongation, major-to-minor axis ratio; (13) DAOphot sharpness parameter; (14) Reddening from Schlafly & Finkbeiner (2011) ; (15) FDS field pointing ID. All morphological quantities from Cols. (8–13) are derived from the *a*-stacks. The full table is available in electronic form at the CDS, and at the web-pages of the project, at: http://fdscat.oa-abruzzo.inaf.it/.

Table 4. Extract of the FDSex *gri* catalog.

ID	RA (J2000)	Dec (J2000)	m_g	m_r	m_i	Star/Gal.	CI_n	F.R.	$FWHM$	Elong.	Sharp.	$E(B-V)$	Field
	(deg)	(deg)	(mag)	(mag)	(mag)			(arcsec)	(arcsec)				(#)
(1)	(2)	(3)	(4)	(5)	(6)	(7)	(8)	(9)	(10)	(11)	(12)	(13)	(14)
FDSJ033332.60-374029.36	53.385815	−37.674820	25.154 ± 0.127	25.010 ± 0.185	24.028 ± 0.175	0.566	1.169	0.64	2.08	1.130	1.797	0.011	18
FDSJ033343.98-374044.61	53.433262	−37.679058	20.012 ± 0.010	19.071 ± 0.006	18.451 ± 0.005	0.956	1.066	0.63	0.97	1.020	0.669	0.011	18
FDSJ033138.97-374012.90	52.912369	−37.670250	24.498 ± 0.077	23.868 ± 0.093	23.171 ± 0.140	0.015	1.228	0.71	2.00	1.490	2.733	0.016	18
FDSJ033539.47-374048.47	53.914478	−37.680130	23.700 ± 0.073	22.854 ± 0.054	22.144 ± 0.042	0.018	1.428	0.94	2.37	1.340	3.798	0.015	18
FDSJ033421.67-374037.64	53.590298	−37.677124	24.604 ± 0.093	24.398 ± 0.112	23.846 ± 0.190	0.125	1.307	0.65	1.86	1.370	2.152	0.013	18
FDSJ033258.65-374024.76	53.244354	−37.673546	24.396 ± 0.074	24.348 ± 0.105	24.330 ± 0.232	0.457	1.111	0.50	1.24	1.120	0.839	0.015	18
FDSJ033118.49-374009.10	52.827042	−37.669193	24.306 ± 0.083	23.514 ± 0.075	22.892 ± 0.088	0.012	1.374	0.92	3.11	1.330	4.176	0.016	18
FDSJ033216.89-374016.07	53.070377	−37.671131	25.622 ± 0.183	24.934 ± 0.170	24.127 ± 0.226	0.474	1.368	0.58	1.14	1.310	2.713	0.016	18
FDSJ033258.88-374023.19	53.245346	−37.673107	25.225 ± 0.144	25.426 ± 0.294	25.130 ± 0.500	0.513	1.013	0.37	0.88	2.190	−1.384	0.015	18
FDSJ033211.86-374023.13	53.049416	−37.673092	24.437 ± 0.096	22.781 ± 0.057	21.589 ± 0.063	0.001	1.441	1.29	3.97	1.390	4.409	0.015	18
FDSJ033157.13-374013.28	52.988060	−37.670353	25.117 ± 0.144	24.759 ± 0.180	24.338 ± 0.269	0.559	1.473	0.80	1.60	1.700	3.462	0.015	18
FDSJ033107.58-374005.39	52.781567	−37.668163	24.658 ± 0.083	23.182 ± 0.051	22.461 ± 0.063	0.798	1.112	0.58	1.55	1.330	1.349	0.016	18

Notes. Columns list: (1) FDS ID; (2) Right Ascension; (3) Declination; (4–6) *gri*-band magnitude with error; (7) Star/Galaxy classifier, CLASS_STAR, from SExtractor; (8) normalized concentration index; (9) Flux Radius, from SExtractor in arcseconds; (10) FWHM in arcseconds; (11) Elongation, major-to-minor axis ratio; (12) DAOphot sharpness parameter; (13) Reddening from Schlafly & Finkbeiner (2011) ; (14) FDS field pointing ID. All morphological quantities from Cols. (7–12) are derived from the *a*-stacks. The full table is available in electronic form at the CDS, and at the web-pages of the project, at: http://fdscat.oa-abruzzo.inaf.it/.

Table 5. Master catalog of GCs.

ID	RA (J2000)	Dec (J2000)	m_u	m_g	m_r	m_i	Star/Gal.	CI_n	F.R.	$FWHM$	Elong.	Sharp.	$E(B-V)$	Field	FCC	p_{GC}	r_h	Source
	(deg)	(deg)	(mag)	(mag)	(mag)	(mag			(arcsec)	(arcsec)				(#)			(arcsec)	
(1)	(2)	(3)	(4)	(5)	(6)	(7)	(8)	(9)	(10)	(11)	(12)	(13)	(14)	(15)	(16)	(17)	(18)	(19)
FDS032625.46-354235.74	51.606079	−35.709927	24.917(0.449)	23.694(0.059)	22.952(0.047)	22.718(0.095)	0.887	1.048	0.45	1.13	1.14	0.565	0.01	20	47	1.0	0.243	P
FDS032626.39-354229.81	51.609943	−35.708279	24.595(0.336)	22.749(0.022)	22.013(0.025)	21.688(0.037)	0.981	0.998	0.52	0.86	1.12	0.141	0.01	20	47	1.0	0.275	P
FDS032627.14-354245.15	51.613079	−35.712543	24.001(0.213)	22.418(0.02)	21.774(0.019)	21.528(0.036)	0.983	1.039	0.49	0.85	1.04	0.304	0.01	20	47	1.0	0.281	P
FDS032627.18-354357.56	51.613262	−35.732655	23.739(0.139)	22.258(0.017)	21.39 (0.015)	21.144(0.024)	0.962	1.017	0.52	0.85	1.06	0.387	0.01	20	47	1.0	0.313	P
FDS032627.23-354125.68	51.613449	−35.690468	24.354(0.238)	23.268(0.039)	22.535(0.031)	22.367(0.065)	0.982	1.101	0.52	0.95	1.06	0.665	0.01	20	47	1.0	0.317	P
FDS032627.27-354237.98	51.613628	−35.710552	24.623(0.332)	24.115(0.083)	23.461(0.074)	23.201(0.124)	0.746	1.056	0.54	1.28	1.17	1.172	0.01	20	47	0.95	0.47	P
FDS032627.38-354224.34	51.614079	−35.70676	24.743(0.404)	23.363(0.039)	22.779(0.039)	22.535(0.078)	0.979	1.029	0.53	1.00	1.13	0.603	0.01	20	47	0.98	0.529	P
FDS032627.66-354441.02	51.615265	−35.744728	23.791(0.134)	22.496(0.02)	21.671(0.018)	21.459(0.029)	0.982	0.987	0.50	0.83	1.05	0.082	0.01	20	47	1.0	0.283	P
FDS032628.10-354356.31	51.617069	−35.732307	24.739(0.291)	23.323(0.039)	22.408(0.032)	22.218(0.059)	0.977	1.036	0.47	0.91	1.05	0.235	0.01	20	47	1.0	0.356	P
FDS032628.17-354359.17	51.617355	−35.733105	25.015(0.486)	23.795(0.058)	23.191(0.055)	22.928(0.086)	0.177	1.637	1.06	3.39	1.43	1.453	0.01	20	47	0.98	0.37	P
FDS032628.20-354425.43	51.617496	−35.740398	24.222(0.194)	24.278(0.081)	23.706(0.095)	23.046(0.113)	0.656	1.115	0.53	1.52	1.21	0.613	0.01	20	47	0.97	0.218	P
FDS032628.34-354341.85	51.618095	−35.728291	25.107(0.395)	24.443(0.102)	23.598(0.075)	23.546(0.185)	0.8	1.048	0.50	1.15	1.14	0.581	0.01	20	47	0.99	0.294	P
...																		
FDS033633.14-345643.64	54.138096	−34.945457	23.595(0.142)	22.007(0.013)	21.226(0.014)	20.954(0.016)	0.921	1.007	0.55	0.86	1.08	0.341	0.015	11	...	...	...	S
FDS033633.49-350248.19	54.139542	−35.046719	24.75 (0.418)	22.906(0.031)	22.175(0.027)	21.732(0.045)	0.984	1.013	0.50	0.88	1.03	0.27	0.014	11	...	...	...	S
...																		
FDS033630.08-350013.69	54.125324	−35.003803	24.466(0.393)	22.079(0.014)	21.266(0.016)	20.862(0.021)	0.926	1.054	0.56	0.95	1.1	0.486	0.015	11	167	1.0	0.381	S+P
FDS033630.10-351753.79	54.125427	−35.298275	22.792(0.066)	21.364(0.009)	20.771(0.012)	20.453(0.019)	0.911	1.084	0.66	1.04	1.53	0.489	0.011	11	170	1.0	0.468	S+P

Notes. Columns list:(1) FDS ID; (2) Right Ascension; (3) Declination; (4–7) *ugri*-band magnitude with error; (8) Star/Galaxy classifier, CLASS_STAR, from SExtractor; (9) normalized concentration index; (10) Flux Radius, from SExtractor in arcsec; (11) FWHM in arcseconds; (12) Elongation, major-to-minor axis ratio; (13) DAOphot sharpness parameter; (14) Reddening from Schlafly & Finkbeiner (2011) ; (15) FDS field pointing ID. All morphological quantities from Cols. (8-13) are derived from the *a*-stacks. (16–18) Fornax cluster catalog ID of the host galaxy, p_{GC} likelihood, and median g and z GC half light radius from Jordán et al. (2015); (19) Source of the confirmed GC: "S" for spectroscopic confirmed GC –from Pota et al. (2018) or Schuberth et al. (2010)–, "P" for photometric confirmed GC from the ACSFCS dataset. The full table is available in electronic form at the CDS.

Table 6. Master catalog of UCDs.

ID	RA (J2000)	Dec (J2000)	m_u	m_g	m_r	m_i	Star/Gal.	CI_n	F.R.	$FWHM$	Elong.	Sharp.	$E(B-V)$	Field	v_{hel}	Source
	(deg)	(deg)	(mag)	(mag)	(mag)	(mag			(arcsec)	(arcsec)				(#)	(km s^{-1})	
(1)	(2)	(3)	(4)	(5)	(6)	(7)	(8)	(9)	(10)	(11)	(12)	(13)	(14)	(15)	(16)	(17)
FDS033854.05-353333.42	54.725212	−35.559284	20.701(0.037)	18.959 (0.042)	18.037(0.041)	17.626(0.036)	0.029	1.321	1.21	1.55	1.04	3.393	0.01	11	1517.0 (6.0)	F08
FDS033805.05-352409.33	54.521023	−35.402592	21.056(0.015)	19.308 (0.007)	18.568(0.009)	18.238(0.007)	0.959	1.024	0.60	0.90	1.13	0.559	0.012	11	1198.9 (6.1)	F08
FDS033935.92-352824.59	54.899654	−35.473499	21.109(0.022)	19.673 (0.027)	19.033(0.022)	18.588(0.013)	0.261	1.163	0.76	1.06	1.06	1.585	0.011	11	1878.0 (5.0)	B07
FDS033806.29-352858.72	54.526222	−35.482979	21.447(0.022)	19.814 (0.017)	19.086(0.022)	18.681(0.014)	0.799	1.137	0.72	1.08	1.26	1.335	0.011	11	1234.0 (5.0)	B07
FDS033703.22-353804.51	54.263435	−35.634586	21.66 (0.025)	19.895 (0.015)	19.12 (0.018)	18.699(0.013)	0.537	1.123	0.72	0.99	1.03	1.482	0.011	11	1561.0 (3.0)	F08
FDS033810.34-352405.79	54.543095	−35.401608	21.653(0.019)	19.987 (0.005)	19.261(0.005)	18.972(0.005)	0.979	0.985	0.54	0.84	1.09	0.131	0.012	11	1626.0 (10.0)	M08
FDS033952.54-350424.04	54.968903	−35.073345	21.342(0.023)	20.018 (0.019)	19.332(0.014)	19.069(0.018)	0.863	1.073	0.74	0.93	1.06	0.955	0.011	11	1236.0 (21.0)	F08
FDS033823.72-351349.49	54.59885	−35.230415	21.515(0.02)	20.13 (0.007)	19.579(0.01)	19.308(0.013)	0.831	1.117	0.62	0.95	1.02	1.129	0.012	11	1637.0 (14.0)	F08
FDS033743.56-352251.47	54.431484	−35.380966	21.616(0.025)	20.16 (0.007)	19.592(0.014)	19.271(0.011)	0.764	1.093	0.65	0.96	1.07	1.214	0.013	11	1420.0 (7.0)	F08
FDS033841.94-353313.03	54.674747	−35.553619	21.944(0.025)	20.194 (0.01)	19.462(0.008)	19.091(0.007)	0.967	1.051	0.57	0.89	1.04	0.578	0.01	11	2024.0 (10.0)	M08
FDS033627.70-351413.84	54.115421	−35.237179	22.214(0.046)	20.198 (0.009)	19.36 (0.02)	18.925(0.02)	0.803	1.171	0.69	1.11	1.14	1.385	0.012	11	1386.0 (4.0)	B07
FDS033920.51-351914.25	54.835464	−35.320625	21.916(0.032)	20.253 (0.02)	19.562(0.025)	19.031(0.013)	0.176	1.174	0.72	1.07	1.03	1.905	0.011	11	1462.0 (5.0)	F08

Notes. Columns list:(1) FDS ID; (2) Right Ascension; (3) Declination; (4–7) *ugri*-band magnitude with error; (8) Star/Galaxy classifier, CLASS_STAR, from SExtractor; (9) normalized concentration index; (10) Flux Radius, from SExtractor in arcsec; (11) FWHM in arcseconds; (12) Elongation, major-to-minor axis ratio; (13) DAOphot sharpness parameter; (14) Reddening from Schlafly & Finkbeiner (2011) ; (15) FDS field pointing ID. All morphological quantities from Cols. (8–13) are derived from the *a*-stacks; (16) Heliocentric velocity from the literature. The full table is available in electronic form at the CDS.

References. K99: Kissler-Patig et al. (1999); M04: Mieske et al. (2004); F07: Firth et al. (2007); B07: Bergond et al. (2007); M08: Mieske et al. (2008); G09: Gregg et al. (2009); S10: Schuberth et al. (2010); P18: Pota et al. (2018).

The spectroscopic sample is a combination of Pota et al. (2018) and Schuberth et al. (2010) datasets. By matching the spectroscopic and photometric catalogs –cleaned up by the common sources– with our FDS *ugri* catalog, we obtained a list of ∼3.250 GCs. We completed our master catalogs of reference compact stellar systems with 68 bright sources in Fornax, confirmed UCD compiled from the available spectroscopic and photometric literature for this class of objects in Fornax. The GC and UCD master catalogs are given in the Tables 5 and 6.

The upper panels in Fig. 8 shows the same color-color diagrams as in Fig. 7 with a zoom over the color-color region of GCs and UCDs. The contour levels of sources from the master catalog are reported with thick dark-blue lines (we adopt linear spacing for contour levels). In the figure we also report the SPoT simple stellar population models (Brocato et al. 1999; Cantiello et al. 2003; Raimondo et al. 2005), for an age range of 4–14 Gyr and metallicity [Fe/H] = −1.3 to 0.4 dex. The consistency between the empirical loci of GCs and stellar population models for the typical age and metallicity ranges of GCs, provides further independent support to the reliability of the calibration approach adopted. In the $(u-r)$–$(g-i)$ plane, the most metal-rich old stellar population models do not match with the observed GC distribution. One possible explanation is the combination of two effects: the small number of observed old GCs with such high metallicity (age ≥ 10 Gyr, [Fe/H] = 0.4, more than twice solar metallicity) and, consequently, the uncertainties of stellar population models is this regime.

The middle and lower panels of the figure also show the $(g-i)$ and $(u-r)$ color histograms for the photometric, spectroscopic and combined samples, for sources brighter than m_g = 23.5 mag. The asymmetric appearance of the color distribution is a consequence of the well-known color bimodality of GC systems in some filters (Ashman & Zepf 1992; Yoon et al. 2006; Blakeslee et al. 2010; Usher et al. 2012; Cantiello et al. 2014), here smoothed as the GC sample is a combination of GCs around ∼30 galaxies in Fornax, each one with different morphological types and magnitudes, hence with different properties in terms of GCs color peaks (Peng et al. 2006).

3.2. GCs and UCDs Selection by shape and photometric properties

At the assumed distance of Fornax, our best resolution for $FWHM_a \sim 0\farcs7$ (e.g., field FDS#1 a-stack) corresponds to a physical size of ∼68 pc. Using specific analysis tools (e.g., Baolab, Larsen 1999), sources down to $\sim FWHM/10$, ∼7 pc for us, are marginally resolved, and can be analyzed and identified as slightly resolved sources. Typical GC half light radii of 2–4 pc are found in Fornax GCs from high-resolution ACS data (Jordán et al. 2009; Masters et al. 2010; Puzia et al. 2014). Using as reference the catalog of Fornax GC candidates by Jordán et al. (2015), ∼0.5% of the best sample ($p_{GC} \geq 0.75$) has an half light radius $r_h \geq 7$ pc estimated in both g and z bands. Hence, even at the best resolution, we can assume the largest fraction of GCs in our catalogs are indistinguishable from point like sources.

To identify compact stellar systems we adopted a procedure similar to our previous works (Cantiello et al. 2018a,b). We relied on several indicators of compactness derived from the multi-band a-stacks, as on such frames we have the lowest field-to-field variation, and, by construction, the best seeing over the entire FDS and FDSex areas. As in previous works, we combined the selection based on CI_n to other morphometric indicators from DAOphot and SExtractor (elongation, flux radius, FWHM, class star, sharpness). This refines and further cleans the final sample of compact sources by the possible outliers not identified by using the sole CI_n, or by any other single indicator.

A comparison of the CI_n distribution for the full *ugri* sample and for the GCs in the master catalog is shown in Fig. 9 (upper left panel). From the comparison with the reference sample (dark contour levels in the panel) we find that the GC locus extends over the $CI_n \sim 1$ line, with a tail toward larger CI_n values at fainter m_g magnitudes. UCDs are also reported in the figure, with black filled dots, and show small but noticeable offsets with respect to the median properties of confirmed GCs, in particular for the size-dependent parameters (like flux radius and FWHM). Such an effect depends on the evidence that UCDs can have effective radii a factor of several times larger than GCs (Mieske et al. 2008; Misgeld & Hilker 2011), i.e. they appear resolved, or slightly resolved, in our multi-band best seeing image stacks.

In Fig. 9, we also show some of the other indicators used to identify GCs, together with UCDs and contour levels of the master catalog for the appropriate diagram. To define the best GC selection intervals for each indicator, we analyzed the master catalog using GCs brighter than m_g = 23.5, and derived the median and the $\mathrm{rms_{MAD}}$ for each indicator. The results are reported in Table 7. In the table we also show the median properties for the reference sample of 68 UCDs.

In addition to morphology, we refine the catalog of candidate compact sources by their photometric characteristics: the shape of the GCLF (or the magnitude interval for known UCDs), the color intervals and the errors on colors.

In our previous works, which have mostly been focused on NGC 1399, we adopted as bright magnitude cut to the GCLF the magnitude $3\sigma_{\mathrm{GCLF}}$ above the turn-over m_g^{TOM} of this bright cD galaxy at the photo-center of Fornax. The Fornax cluster, with an estimated total line of sight depth of ∼2 Mpc (Blakeslee et al. 2009), has member galaxies located at different physical distances. Adopting the ACSFCS results, the median g-band GCLF turn-over magnitude and σ_{GCLF} values are $m_g^{\mathrm{TOM}} = 24.03 \pm 0.15$ mag and $\sigma_{\mathrm{GCLF}} = 0.94 \pm 0.11$ mag (Jordán et al. 2007). A $3\sigma_{\mathrm{GCLF}}$ cut above the median TOM corresponds to $m_g \sim 21.2$ mag. For a rough estimate of the number of GCs lost with such bright cut level, we again take as reference the ACSFCS full list of GCs hosted by 43 Fornax galaxies (Jordán et al. 2015). The list contains 53 GCs brighter than m_g = 21.2 mag (∼0.8% of the sample[9]). Hence, in what follows we assume m_g = 21 mag as bright cut of the GCLF, which includes 99.5% of the likely GCs sample in the ACSFCS sample. The bright cut is needed for having a sample of GC candidates with lower stellar contamination, at the cost of an expected minimal impact on the GC population. We will in any case also analyze candidates within $19.0 \leq m_g \leq 21.0$ mag, the magnitude interval corresponding to UCDs in Fornax (Mieske et al. 2012). These systems share many characteristics with GCs but, as mentioned above, have larger effective radii than GCs (see Fig. 9).

As a maximum color uncertainty, we chose $\Delta(g-i)_{\mathrm{max}} = 0.15$ and $\Delta(u-r)_{\mathrm{max}} = 0.3$, corresponding approximately to half of the separation between the blue and red peaks of the GCs color sub-populations host in typical bright galaxies (Cantiello et al. 2018a).

Thanks to the multiple color coverage, the selection of candidates can be improved using color-color criteria, rather than flat single-color ranges. The contour levels in the color-color

[9] Some even brighter GCs are missed in the ACSFCS, as shown by Fahrion et al. (2019a).

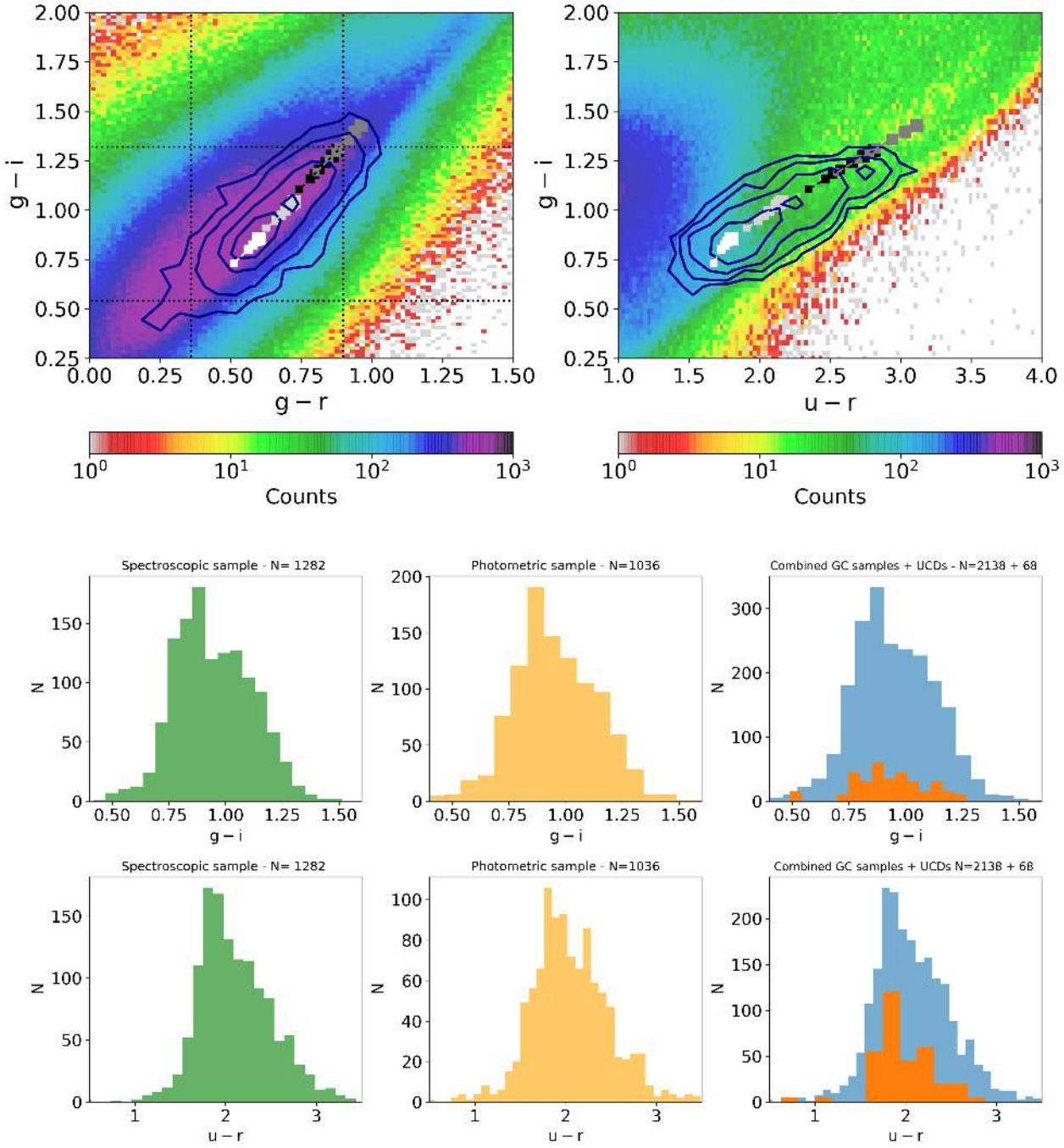

Fig. 8. *Upper panels*: color–color Hess diagrams for the sample of sources with *ugri* photometry, over the color interval expected for GCs and UCDs. The dark-blue lines show the linear spaced contour levels of sources in the master GC catalog. Filled squares show the integrated colors from the SPoT stellar population synthesis code. White, light-gray, black, and dark-gray symbols indicate metallicity [Fe/H] = [−1.3, −0.7, 0.0, 0.4], respectively; symbols size scales with increasing model age, ranging between 4 and 14 Gyr, with 2 Gyr step. Same metallicity models are connected with dashed lines. *Left color-color panel*: we also draw with dotted lines the color intervals of GCs assuming $\pm 3-\mathrm{rms}_{\mathrm{MAD}}$ with respect to the median values in Table 7. *Middle and lower panels*: $(g-i)$ and $(u-r)$ color histograms, respectively, for the master spectroscopic (*left panel*, green histogram), photometric (*middle*, yellow), and combined (*right*, blue) GC catalogs. In the third histograms the data of UCDs are also shown (orange), expanded by a factor of five for sake of clarity. Only sources brighter than $m_g = 23.5$ mag are considered.

diagrams of Fig. 8 reveal the relatively narrow color-color loci of GCs. A simple color-color selection box (e.g., black dotted lines in the upper left panel of the figure) would imply a trivial contamination from either stars or background objects. Instead, we proceed by inspecting in the color-color planes all sources satisfying the morpho-photometric parameters identified above. Finally, only the sources inside the color-color contours of the reference sample are identified as candidates and used for further analysis (see next section).

In summary, to identify the least contaminated and most complete possible GCs (and UCDs) catalog from our photometry, we adopted a three step strategy. First, we generated a master GCs (and UCDs) catalog using confirmed sources in the literature. From the GCs catalog we cut out all sources fainter than

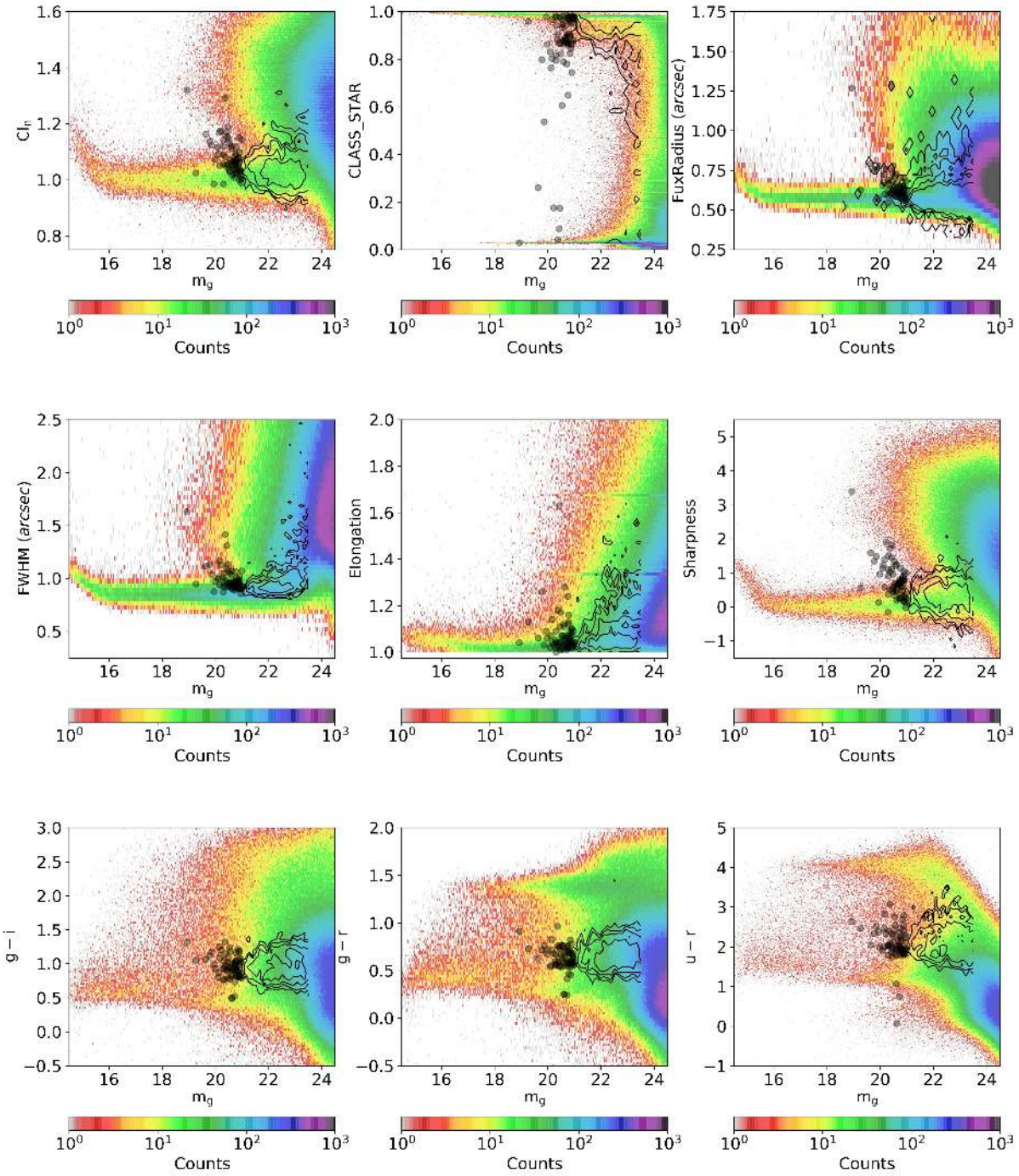

Fig. 9. Hess diagrams of several morphometric and photometric indicators used to select GC candidates, overlaid with the contour levels of GCs in the master reference catalog, and UCDs (black circles).

$m_g = 23.5$ mag, to better identify the morpho-photometric loci of GCs; the cut is adopted only for the reference catalog, for the GC identification and analysis on the FDS catalogs, we adapted a ∼1 mag fainter limiting magnitude to increase the sample of GC candidates (see below). Second, we used the control parameters shown in Fig. 9 and the properties of the master catalogs to define the best intervals for GCs and UCDs selection. These selection criteria are then independently applied to the FDS and FDSex catalogs. For some parameters, we adopted as confidence intervals the ranges from the master catalogs, using the median $\pm N \times \mathrm{rms}_{\mathrm{MAD}}$, with $N = 4/2$ for GCs/UCDs respectively (median and rms from Table 7); for the GCLF, colors, and color errors, we proceeded as described above. The complete list of parameters, together with the used ranges, is reported in Table 8. Third, the sample of compact sources after the previous steps was inspected in the color-color plane to further narrow down the contamination using the contour levels derived from the master catalog.

3.3. Surface distribution of compact sources over the FDS area

The analysis of the GCs over the FDS and FDSex area, together with the comparison with similar datasets, will be presented in

Table 7. Median properties of the GCs and UCDs in the reference catalog.

	GCs		UCDs	
Indicator	Median	$\mathrm{rms_{MAD}}$	Median	$\mathrm{rms_{MAD}}$
$(g-i)$	0.93	0.13	0.94	0.12
$(g-r)$	0.63	0.09	0.64	0.08
$(u-r)$	2.02	0.26	2.03	0.21
CI_n	1.03	0.03	1.06	0.03
CLASS_STAR	0.96	0.03	0.88	0.08
$FWHM$ ($''$)	0.94	0.08	0.91	0.04
Flux radius ($''$)	0.55	0.03	0.60	0.03
Elongation	1.09	0.05	1.04	0.02
Sharpness	0.32	0.26	0.69	0.34
N_{sources}	2138		68	

Table 8. Photometric and morphometric parameters adopted for source selections.

	GCs		UCDs	
Indicator	Min.	Max.	Min.	Max.
m_g	21.0	24.5	19.0	21.0
$(g-i)$	0.5	1.4	0.5	1.4
$(g-r)$	0.25	1.1	0.25	1.1
$(u-r)$	1.2	3.4	1.2	3.4
CI_n	0.90	1.17	1.00	1.13
CLASS_STAR	0.50	1.00	0.5	1.00
$FWHM$	0.62	1.26	0.8	1.12
Flux radius	0.42	0.68	0.5	0.8
Elongation	...	1.30	...	1.5
Sharpness	−0.75	1.40	0.3	2.0
$\Delta(g-i)$	...	0.15	...	0.15
$\Delta(u-r)$	...	0.30	...	0.30

more detail in a forthcoming paper. In the following, we show a preliminary determination of GCs and UCDs surface density maps as an example use of the FDS catalogs, based on the source selection strategies described in the previous section; in Sect. 4, we also show an example of use of the catalogs for the study of background galaxies.

3.3.1. Globular clusters and UCDs distribution maps

Using the identification scheme described above, we inspect the GC distribution maps over the FDS and FDSex areas using as reference the *ugri* and *gri* selections, respectively.

GC candidates are derived by cross-matching the color-color regions of pre-selected GC candidates (Table 8), with the color-color loci of GCs identified in the master sample. Candidates falling in the contour levels of higher GCs density in the two-color diagram have higher likelihood of being true GCs. However, the narrow color-color range also implies lower completeness. In what follows, then, we analyze the GC density maps for candidates over different color-color contour levels.

Figure 10 shows the two-dimensional projected distribution over the ∼21 sq. degree area of FDS. In the left panels of the figure we plot the color-color Hess diagrams of all sources identified with the selection criteria in Table 8, overplotting the contour levels of the GCs in the master sample. Even after all morpho-photometric cleaning of the sample (except for the color-color selection), a substantial fraction of selected candidates lies outside the expected GCs color-color region identified by the contour levels in the panel.

The middle and right panels of Fig. 10 show the maps of GCs identified adding also the color-color contour level selection, that is, of all sources falling in the contour levels marked in the left panels of Fig. 10. Each row of panels in the figure refers to a different contour level, indicated by the thick magenta contour in the left panel. Again, the inner contours pinpoint regions with higher GCs density in the color-color diagram, thus the level of contamination from non-GCs decreases in the maps from the upper to lower panels in Fig. 10; vice-versa, because of the smaller color-color intervals, lower panels suffer due to higher incompleteness fractions. In particular, the lowermost panel is limited to a blue color-color region, hence mostly representative on the blue-GCs sub-population, also discussed below.

We calculate the smooth density maps using non-parametric kernel density estimates based on FFT convolution[10]. After various tests, we adopted a grid mesh size of ∼0.1′ spacing, smoothed with an Epanechnikov kernel, with kernel bandwidth[11] five times the grid size.

Although obvious differences appear between GC maps drawn from the diverse color-color contour levels, there are several recurrent patterns appearing at various levels of selection, that is at different levels of GC contamination and incompleteness. The recurrence of the sub-structures over various GC color-color contours supports the reality of the sub-structure itself. Some of these patterns were also discussed in our works (D'Abrusco et al. 2016; Cantiello et al. 2018a), over a smaller survey area and using partially different data and algorithms; yet, here we observe several new features, that are possible extensions to those described previously.

Central over-density. For sake of clarity, in Fig. 11, we plot the density map relative to the third contour plot (third row in Fig. 10). The peanut shaped distribution of GCs, elongated in the E-W direction of the cluster, with a marked peak on NGC 1399, was already found in our studies relying on data of the central FDS area, within $52.5 \leq \mathrm{RA\ (deg)} \leq 56.5$ and $-37 \leq \mathrm{Dec\ (deg)} \leq -35$ (a total of ∼7.5 sq. degrees).

In the new dataset, covering about four times the area previously inspected, we find a ∼10 deg tilt of the position angle for the broad distribution of inter-galactic GC candidates, tilting in the direction of NGC 1336 (the tilt direction is also indicated with a blue dashed line in Fig. 11). The length of the last isodensity contour is $a = 2.6 \pm 0.2$ deg (or 920 ± 60 kpc), obtained combining the sizes from the four maps in Fig. 10. The width of the distribution is of $b = 0.89 \pm 0.03$ deg (or 310 ± 10 kpc), implying an ellipticity $\epsilon = 1 - b/a \sim 0.65$, slightly larger than what was previously found on smaller scales (Kim et al. 2013; Cantiello et al. 2018a).

F & G features. In the distribution, aside from the obvious case of NGC 1399 and its fainter close companions, we observe several regions of marked over-density in correspondence with bright galaxies or pair of galaxies: NGC 1427, NGC 1374/1375, NGC 1351, all with $B_T \leq 12$ mag, and of NGC 1336, which is ∼1.5 mag fainter than the others. The GCs peaks on these

[10] We used the KDEpy python 3.5+ package, which implements several kernel density estimators. See the web pages of the package for relevant literature: https://kdepy.readthedocs.io/en/latest/API.html#fftkde

[11] Using a Gaussian kernel, the bandwidth is equivalent to the σ of the distribution.

regions were already commented in our previous works. However, thanks to the larger area analyzed and the different detection strategy the new photometric sample reaches ∼1 mag deeper u-band, we now find that such structures are connected and extend to larger clustercentric radii. The F and G features described in D'Abrusco et al. (2016) (arrows in Fig. 11) extend ∼ 1.5 degrees (∼0.5 Mpc) South-West and North-East of the cluster core, respectively. These substructures do not cross any galaxy brighter than $B_T = 16$ mag, both overlap a handful of galaxies with $16 \leq B_T \leq 18$ mag (absolute magnitude $-15.5 \leq M_{B,\rm tot}$ (mag) ≤ -13.5), and a dozen of fainter galaxies, down to $B_T \sim 20$ mag ($M_{B,\rm tot} = -11.5$ mag). The F extension, points toward a group of five galaxies with magnitudes B_T between 13.5 and 16 mag, dominated by ESO 358-050, where no GC structure or overdensity is noticeable in any of the GC color-contour selections.

The level of persistence of the F and G structures changes with the selection contours. To estimate the level of significance of both these overdensities we proceed as follows. First, taking as reference the third contour level in Fig. 10, we count the number of GC candidates in the F and G feature density contours (N_X, with X referred to the F or G region). Then, to define a background level, we move the same density contours around the FDS area, avoiding the central overdensity and the regions with galaxies brighter than $B_T \sim 16$, and count the number of candidates in such regions. For each feature, we identified seven independent regions for background estimation over the survey area; then we used the median and $\rm rms_{MAD}$ of the GC number counts in the seven regions ($N_{X,\rm back.}$, $\rm rms_{X,back.}$) to quantify the F and G overdensity ratio as follows:

$$\Sigma[(\rm in-out)/err] = (N_X - N_{X,\rm back.})/(\rm rms^2_{X,back.} + \delta N_X^2)^{1/2}.$$

By definition, Σ[(in−out)/err] quantifies the ratio between the difference of counts in and out the X feature, and the squared sum of the standard deviation of both counts, assuming a poissonian fluctuation for N_X ($\delta N_X = N_X^{1/2}$). We obtain Σ[(in−out)/err] ∼ 4.2, for F and ∼4.4 for G, meaning that the GC candidates overdensity, with respect to the diffuse background GCs component, is at least factor of four larger than the estimated total expected counts fluctuation in both regions. A similar result, albeit for smaller regions, with a different (shallower) sources catalog and with independent algorithms, was found by D'Abrusco et al. (2016).

The F is more evident in the wider color-contours selections (upper two panels in Fig. 10), which also include the red GCs that are mostly expected to be closely bound to the galaxies; because of the wider selection intervals, this feature is also likely to have higher fore or back-ground contamination. The G structure, instead, appears more connected to the blue GC population (lowermost panel in the figure); the properties of such coherent structure extending over cluster scale, over an area devoid of bright galaxies and composed mostly of blue GCs –the GC subpopulation typically found in the outer galactic regions– suggest its inter-galactic nature. We speculate that the G feature might be connected with NGC 1404, as a stream of blue GCs possibly leading or tailing from the galaxy; the galaxy has an overall z-band specific frequency $S_{N,z} = 0.30 \pm 0.00$, and within one effective radius $S_{N,z,\rm In} = 0.12 \pm 0.01$ (Liu et al. 2019). The whole median of the ACSFCS sample is $\langle S_{N,z} \rangle = 0.82 \pm 0.37$, or 0.93 ± 0.26 if limited to the five brightest galaxies in the main Fornax cluster after excluding NGC 1399 and NGC 1404 itself[12]; for the $S_{N,z,\rm In}$ from the combined Fornax and Virgo cluster sample (Table 4 in Liu et al. 2019), and limited to galaxies brighter than $M_z \sim -20.7$ mag, we obtain $\langle S_{N,z,\rm In} \rangle = 0.32 \pm 0.18$. Hence, in all cases NGC 1404 is a noteworthy case of bright galaxy with a GC population consistently lower than average. Bekki et al. (2003) have a dynamical model for the GCs system of NGC 1404, explaining its low specific frequency as an effect of the tidal stripping of GCs by the gravitational field around cluster core, dominated by NGC 1399. The authors find that at given models input conditions (highly eccentric orbit, initial scale-length of the GCs system twice as large as the galaxy effective radius), NGC 1404 GCs population can be reduced through stripping to the presently observed value. One of the observable characteristics predicted by Bekki et al. is the formation of an elongated or flattened tidal stream of GCs.

Furthermore, the complex structure of the Fornax X-ray halo (Paolillo et al. 2002; Su et al. 2017) has been explained by Sheardown et al. (2018) using hydrodynamics simulations, by the orbital motion of NGC 1404 within the cluster, assuming that the galaxy is at its second or third passage through the cluster center.

NGC 1336. The new photometry confirms the peculiarity of NGC 1336 with respect to the rest of the cluster: we find its GCs overdensity (E feature in D'Abrusco et al. 2016) isolated with respect to the rest of the cluster-wide GCs system. The distinctiveness of NGC 1336 is also discussed by Liu et al. (2019), who find that it has the second highest GC specific frequency, after NGC 1399, and the largest 3D clustercentric distance in the ACSFCS sample. The relative isolation of the galaxy from the Fornax core, at ∼2 times of the cluster virial radius, also supported by the lack of GC streams toward the core, might strengthen the hypothesis by Liu et al. that it is an infalling central galaxy with a higher total mass-to-light ratio, resembling the behavior of the most massive ETGs. Its GC system has possibly experienced fewer external disruption processes, and the GCs may have a higher survival efficiency. The presence of two kinematically decoupled cores (Fahrion et al. 2019b), most probably evidencing a major merger that has altered the structure of NGC 1336 significantly, might further support such hypothesis.

The C feature. A further structure, labeled C in D'Abrusco et al., ranges from NGC 1380 North-West in the direction of the ringed barred spiral NGC 1350. The feature appears less coherently connected than the F and G in the maps of Fig. 10, and it crosses four galaxies with $B_T \leq 16$, thus, it might be the result of the projected superposition of several adjacent GC systems, rather than an intra-cluster GCs structure.

Blue and red GCs, foreground stars. We also plot the map of blue and red GC candidates in Fig. 12, using the color-contours shown in the left panels. To improve the blue and red GCs separation, taking advantage of the availability of two colors, the separation between red and blue GC is taken from a linear fit to the $(u-r)$–$(g-i)$ sequence of the master GC sample, then taking the blue/red separation from the dip in the distribution projected along this axis, a procedure we already used in Angora et al. (2019, see their Fig. 7, upper panel). The blue and red surface density maps show the property already anticipated above of red GCs being concentrated on galaxies, especially on bright ellipticals, and blue GCs covering a wider area, including the intra-cluster regions.

For comparison with the previous maps, Fig. 13 shows the stellar density map, where stars are identified as the bright sources $16 \leq m_g$ (mag) ≤ 20.5, with the same photo-morphometric properties of GCs (Table 8) except no color

[12] The median with NGC 1399 and NGC 1404, doesn't change notably, being 0.93 ± 0.41.

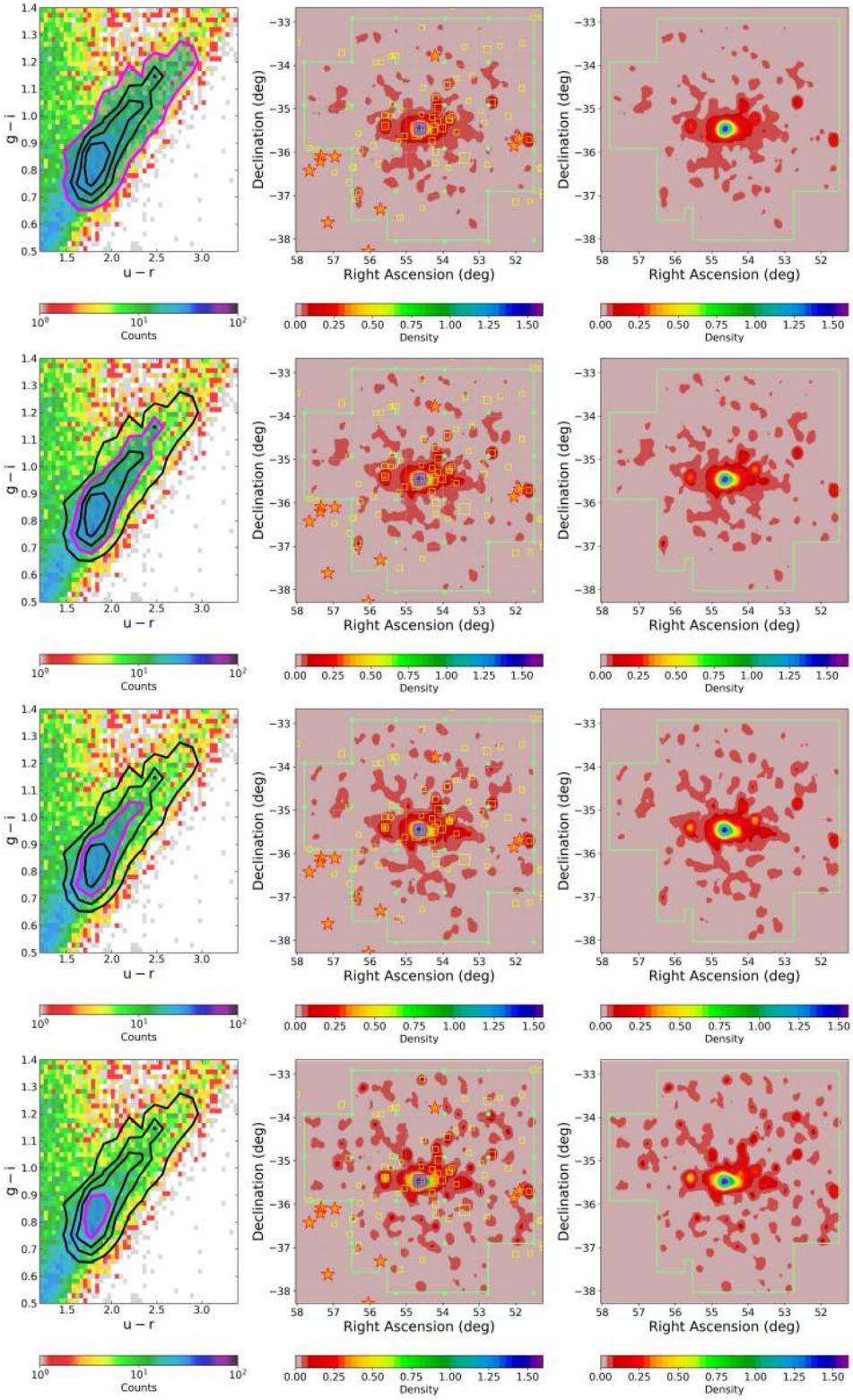

Fig. 10. Surface density maps of GC candidates over the FDS area. *Upper left panel*: color-color Hess diagram for GC candidates selected using the parameters in Table 8. The contour lines refer to the master GC sample. All GC candidates in the color-color contour level shown with a thick magenta solid line (also evidenced with a gray shaded area) are used for the density maps in the middle and right panels. *Upper middle panel*: density map of the GC candidates within the shaded area highlighted in the left panel. The density is in number of candidates per square arcmin. East is left, north is up. The light green line shows the FDS footprint; filled green dots mark the limits of single pointings; five pointed stars mark stars with $m_V \leq 7$ mag; yellow squares show galaxies brighter than $B_T = 16$ mag, with symbol size scaled to galaxy total magnitude; NGC 1399 is also marked with a magenta empty square. *Upper right panel*: as upper middle panel, except that all reference sources and lines are not plotted to highlight the GC structures in the area. *Second to fourth row of panels*: as upper row, but for the other narrower contour levels of the color–color diagram, as evidenced with the magenta contour in the first column of panels. *From upper to lower panels*: the number of GC candidates within the color–color region identified with magenta contour level is: 5.650, 3.650, 2.170, and 900, respectively.

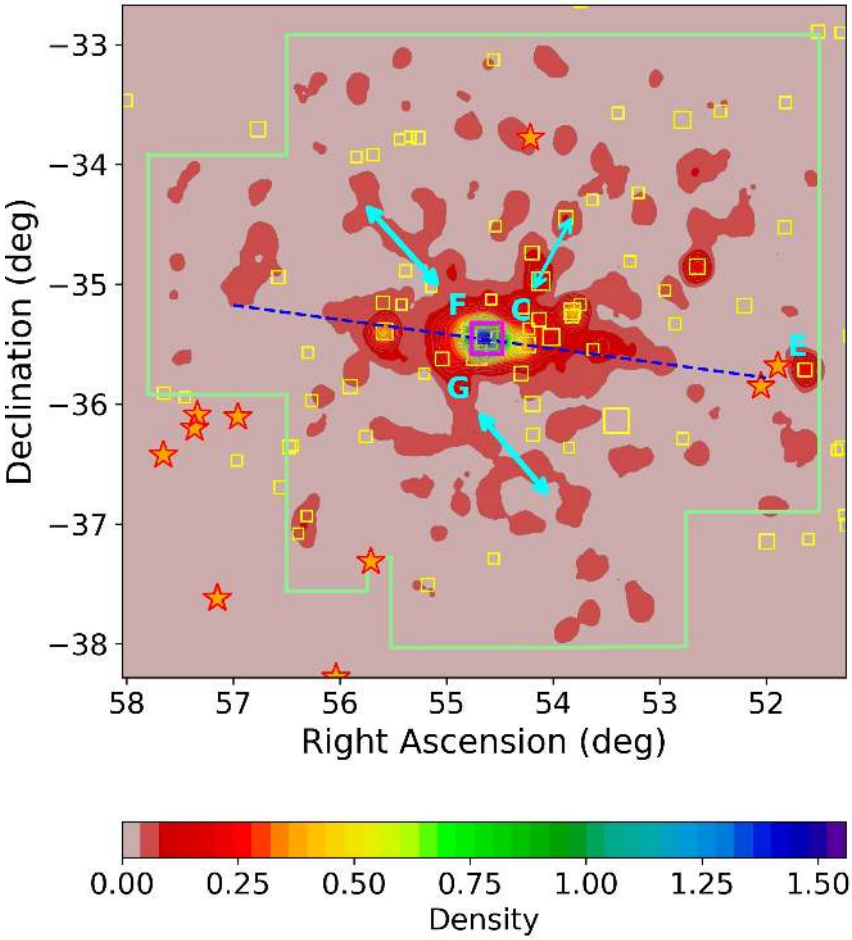

Fig. 11. Single-panel view of the 2-D GC surface distribution. Iso-density contours and symbols are the same as in Fig. 10 (third contour level plots). Light blue arrows and labels indicate the GC over-densities discussed in the text. The blue dashed line shows the ∼10° tilt in the direction of NGC 1336 ("E" label in the figure).

selection is applied. The stellar map shows both the lack of any obvious structure over the field, and the large contamination from MW stars: the map, limited to the brightest part of the field MW stellar population, is derived from ∼23.000 stars, versus the ∼5.600/900 GCs used for the GC maps in Fig. 10, and the ∼2.200/1200 blue/red GCs selected for the maps in Fig. 12.

UCD galaxies. A further map from the *ugri* catalog is shown in Fig. 14, with the UCD surface density distribution over the FDS area, derived using the selection parameters for UCDs, reported in Table 8, and the color contours of known UCDs from the reference sample (magenta solid lines in the figure). Unsurprisingly, the surface density maps show the concentration of UCDs rises around the central square degree area of NGC 1399. The map is mostly shown for completeness, as number of UCDs is known to be small, so even a small contamination can significantly alter the analysis. With our selection we identify 160 sources, which probably include a substantial fraction of contaminating stars, especially in the brightest magnitude bin ($19 \leq m_g \leq 20$), and bright GCs with morphological parameters consistent with the UCDs. Inspecting separately the maps of bright or faint UCDs candidates, adopting $m_g = 20$ mag as the separation limit, we observe that the map for the faint magnitude bin – $m_g = 20$–21 containing 105 candidates at the given selection criteria doesn't change notably with respect to Fig. 14 and it shows an elongated density structure with a peak close to the cluster core, along with two secondary maxima at [RA, Dec] = [53.7, −37.6] and [52.3, −33.5]. The map of the bright component – $m_g = 19$–20, 55 candidates – does not show any noteworthy pattern, with sources appearing evenly distributed in the region, a behavior suggesting large contamination from MW stars in this magnitude range. The study of the UCD distribution over the area requires a dedicated analysis to characterize and identify all the selected UCD candidates, which is beyond the scopes of this study, and will be addressed in a forthcoming work, also using near-IR photometry (Saifollahi et al., in prep.).

In conclusion, it is worth highlighting that all the substructures described in this section are relatively insensitive to the main parameters chosen to identify GC or UCD candidates, and to the details of the algorithms used to derive the maps themselves, except minor details which leave unaltered the general presentation above.

3.3.2. GCs distribution maps over the FDSex area

The lack of *u*-band photometry over the FDSex area implies that any sample of compact sources selected in the area using the same procedures adopted in the previous section, yet based only on *gri* photometry, is more contaminated. In Fig. 15, we plot the contour levels of the master GC sample (blue lines and shaded area), and the contour levels of compact (green color, $CI_n \sim 1$) and extended (red colors, $CI_n \geq 1.3$) sources, all brighter than $m_g = 22.5$ mag, using the *ugri* catalog. The bright magnitude cut is adopted to reduce the scatter due to increased photometric errors at fainter magnitudes. The diagrams show that the sequence of GCs/UCDs/stars in the $(g-i)$–$(g-r)$ matches with the sequence of extended objects, while in the $(g-i)$–$(u-r)$ diagram the degeneracy is less dramatic, maximizing the efficiency of the separation of compact extended sources.

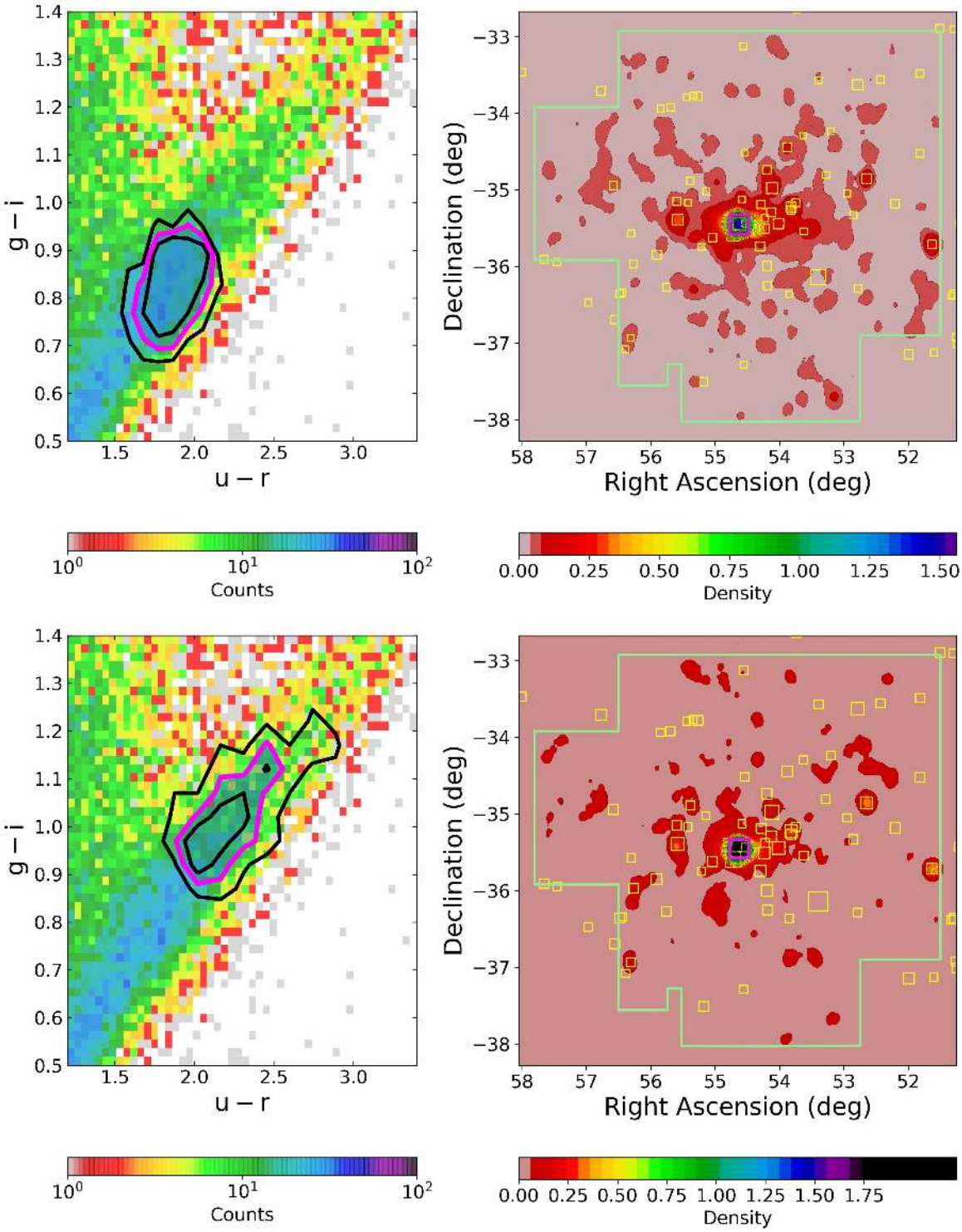

Fig. 12. Two-dimensional density maps of blue (*upper panels*) and red (*lower panels*) GC candidates. Symbols are the same as in Fig. 10.

To obtain a rough estimate of the increase of contamination due to the lack of *u*-band photometry we proceed as follows. Using the *ugri* catalog in the FDS area, we adopt the GC selection scheme described in the previous section but use the $(g-i)$–$(g-r)$ color combination, instead of the $(g-i)$–$(u-r)$, for the selections on the color-color plane. By comparing the number of GC candidates identified using the $(g-i)$–$(u-r)$ color–color, $N^{\rm GC}_{ugri}$, with the number of candidates identified using $(g-i)$–$(g-r)$ color-color, $N^{\rm GC}_{gri}$, we find $(N^{\rm GC}_{gri} - N^{\rm GC}_{ugri})/N^{\rm GC}_{gri} \sim 0.48$. Therefore, this single change in the criteria for GC selections implies the number of sources identified as GC candidates is nearly doubled over the FDS area. Such increase is not spatially uniform: it is close to ∼80% in background regions, that is, far from bright galaxies and their host GC system, and drops to ∼15% around bright galaxies. This difference shows that GC selection in the central cluster area, where GCs have a high surface density, is already quite efficient with a 3-band combination. In contrast, the addition of the *u*-band makes a significant difference in GC

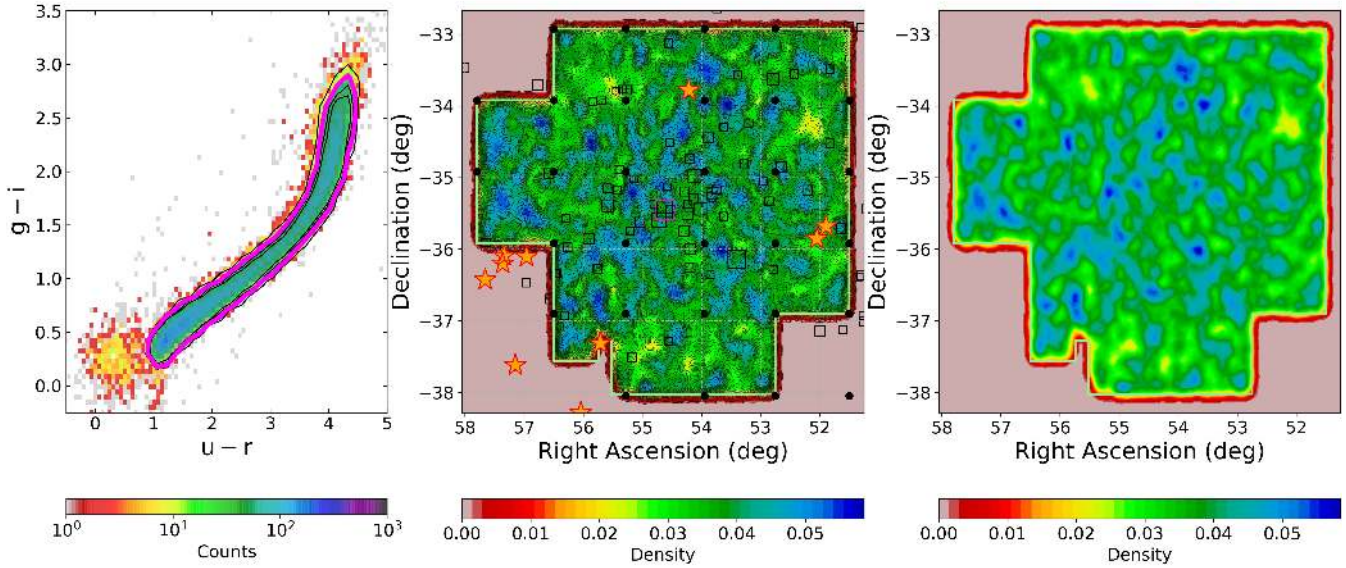

Fig. 13. Surface density maps of bright stars. Symbols are the same as in Fig. 10.

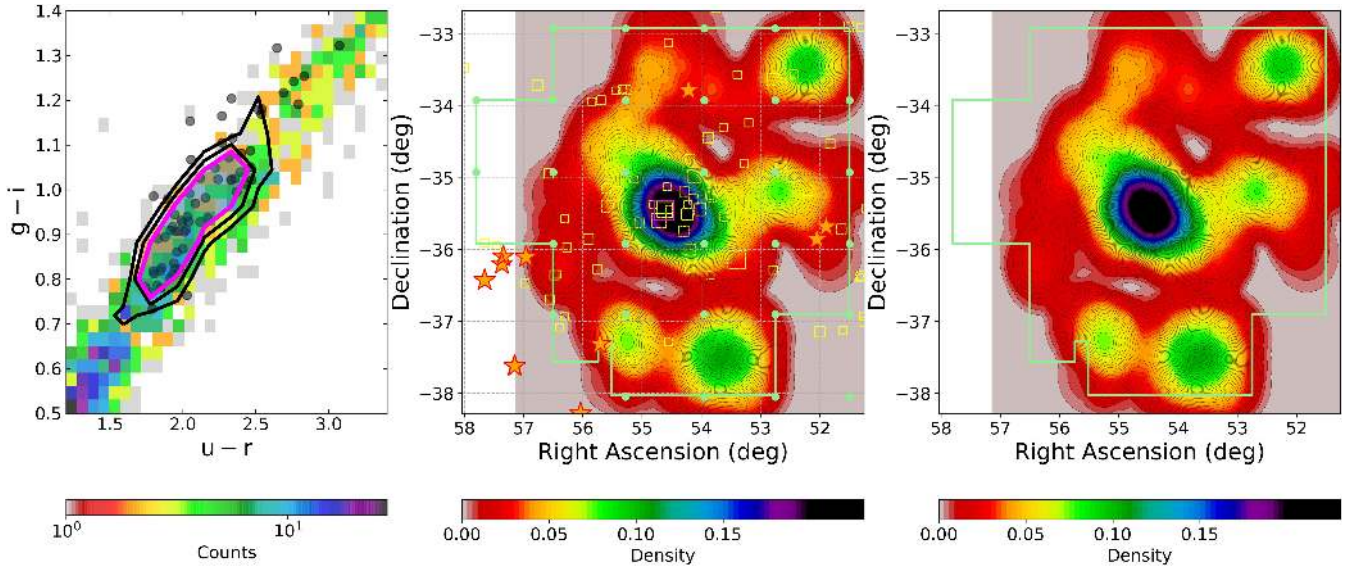

Fig. 14. Surface density maps of UCD candidates. Symbols are the same as in Fig. 10.

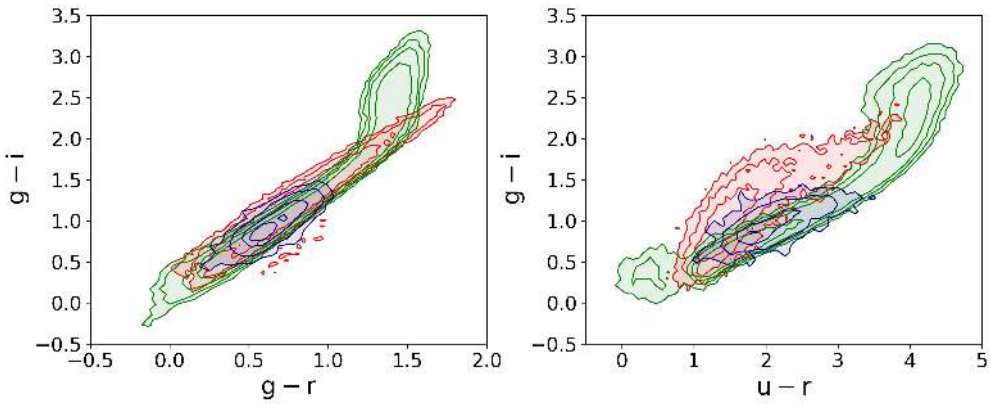

Fig. 15. Color–color contour plots of the GC master catalog (blue contours and shaded area), of point-like sources (green) and of extended sources (red).

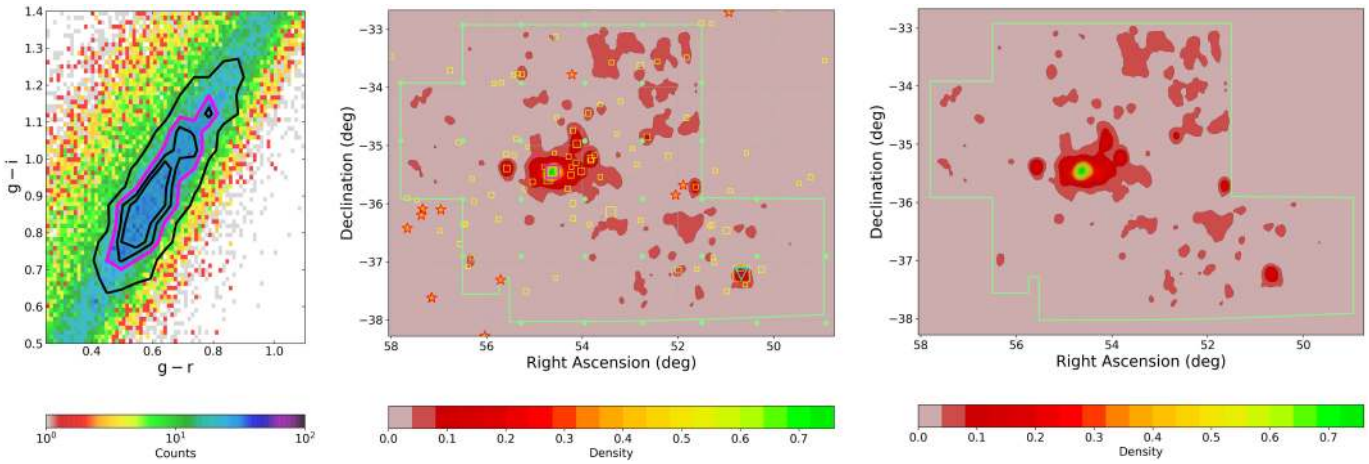

Fig. 16. Same as in Fig. 10, except that over the FDSex area, and the $(g-i)$–$(g-r)$ color-color diagram is used for GCs selection. The position of NGC 1316 is shown with light-blue empty triangle in the middle panel.

selection in the outer parts of the cluster where the fractional background contamination, mostly due to MW stars, is higher.

In spite of the higher level of contamination, the FDSex *gri*-band catalog also includes the area of NGC 1316, Fornax A, the brightest galaxy in the cluster in optical bands, a peculiar giant elliptical, suggested being in its second stage of mass assembly (Iodice et al. 2017b). It is then of particular interest to show here, for the first time, the global properties of the GCs over such wide area. We should, however, be aware that NGC 1316 is known to contain relatively young GCs (∼2 − 3 Gyr, e.g. Gómez et al. 2001; Goudfrooij et al. 2001; Sesto et al. 2017), which are not part of our reference sample. Young GCs are in general bluer and brighter than equally massive old GCs; hence, we bear in mind that our selection is intrinsically biased toward old GCs.

Using the same procedures described in the previous sections, except that $(g-r)$ is used instead of $(u-r)$, we analyze the surface distribution maps over the 27 sq. degrees of the FDSex area. For sake of clarity, in Fig. 16 we only show the second color-color density contour, corresponding to the iso-density contour level of 15 GCs from the master catalog. In the panels of the figure, no obvious GC substructure appears bridging the core of the main Fornax cluster to the Fornax A sub-group. The two brightest galaxies, NGC 1399 and NGC 1316, are ∼3.6 deg apart (∼1.3 Mpc in projection) and the density map of the ∼10.200 GCs selected does not reveal any hint of residual GC tails along the direction connecting the bright ellipticals, with the possible only exception of the East-West elongation of GCs around the cluster core still visible in the *gri* map, although with less details compared with the *ugri* maps.

The higher level of contamination of the *gri* maps appears in some spurious features. Figure 16 shows a structure around the area of coordinates [RA = 52 deg, Dec = −34 deg], characterized by nearly the same geometric appearance of the FDS fields #14, #19 and #31. Such structure is completely unseen in the *ugri* maps which also cover the area; inspecting the three FDS fields we find slightly deeper limiting magnitudes and slightly poorer source compactness relative to the neighboring fields: combined, two effects generate larger number of detections with poorer morphologic characterization, hence a higher fraction of GCs contamination.

To have a less contaminated sample, we narrowed the sample of GC candidates by using a brighter magnitude cut, more stringent ranges on the various morphological parameters in Table 8, and narrower color-color regions. Using narrower selections, the spurious structure around the fields FDS#14/19/31 disappears. Nevertheless, no matter how much the GC sample is narrowed with more strict selections, no GC substructure emerges along the NGC 1316/NGC 1399 direction.

By counting the number of GCs candidates within a given radius centered on each of the two bright galaxies within the respective environments, we find that the number of GCs around NGC 1399 outnumbers NGC 1316 by a factor of 4–4.7 at galactocentric radii $R_{\rm gal}$ of ∼6′ and ∼24′, and by a factor of ∼3 out to $R_{\rm gal} \sim 40'$. Figure 17 shows the number ratio $N^{\rm Sources}_{\rm ratio}(\leq R_{\rm gal}) = N^{\rm Sources}_{N1399}/N^{\rm Sources}_{N1316}$ versus galactocentric distance for GCs candidates (black line in the figure), for galaxies brighter than a given limit (as labeled in the figure), and the flux ratio of the *r*-band integrated magnitudes of the two galaxies (from Iodice et al. 2016, 2017b).

The median $N^{\rm galaxies}_{\rm ratio}$ for galaxies in the range of 6′ − 24′ is ∼2.0 with $\rm rms_{MAD} = 0.3$. Assuming a nearly uniform contamination of the FDSex catalogs around the two regions, we estimate the overdensity of GCs around NGC 1399 compared to NGC 1316 ($N^{GCs}_{\rm ratio} \sim 4$) is a factor of ∼2 larger than the overdensity of galaxies in the magnitude range $11.5 \leq B_T$ (mag) ≤ 16.5 ($-20 \leq M_{B,\rm tot}$ (mag) ≤ -15). Hence, even accounting for the larger density of bright and faint galaxies of all morphological types, the population of GCs is considerably larger in the region of $6' \leq R_{\rm gal} \leq 24'$ around NGC 1399 compared with NGC 1316, and mainly composed of blue GCs.

This overpopulation of GCs is likely associated with the intra-cluster GCs component; on the contrary, the relative GCs under-density around Fornax A, and the lack of any major accretion events of NGC 1316 that could have significantly increased the specific frequency of blue GCs, is possibly at the basis of the lack of any significant GC substructure. Furthermore, as expected from the known factor of ∼2 higher total magnitude of NGC 1316 compared to NGC 1399, the *r*-band flux ratio between the two ellipticals is ∼0.4 ± 0.1 (light–blue line in Fig. 17), a factor of 8−10 lower than the GCs count ratio.

Figure 17 also shows some other features : (a) the GCs and bright galaxies with $B_T \leq 11.5$ mag and $B_T \leq 13.5$ mag ($M_{B,\rm tot} = -20$ and -18 mag, respectively) have $N^{\rm galaxy}_{\rm ratio} \sim 3$ at $R_{\rm gal} \geq 30'$,

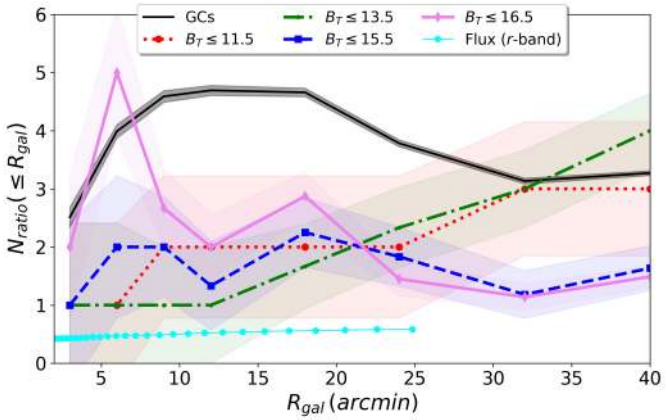

Fig. 17. Number ratio of the total number of sources around NGC 1399 and NGC 1316 within a given galactocentric radius in the respective environment: $N_{\rm ratio}(\leq R_{\rm gal}) = N^{N1399}_{\rm Sources}/N^{N1316}_{\rm Sources}$. The number ratio for GCs is shown with a black solid line; number ratios for galaxies at a given bright magnitude cut are also shown, and labeled. The *r*-band flux ratio between the two galaxies within $R_{\rm gal}$ is shown with light-blue solid line and pentagons.

while for the fainter galaxy bin limits we find $N^{\rm galaxy}_{\rm ratio} \sim 1.3$; (b) the nearly flat GCs $N_{\rm ratio}$ within $9 \leq R_{\rm gal}\,(') \leq 20$, which assumes a value of 4.66 ± 0.04. A more detailed analysis of such properties combined with the data in other galaxy clusters is in progress (Cantiello et al., in prep.).

4. FDS catalogs of background sources and related science

The depth and spatial resolution of the FDS images, together with ancillary data from other spectral ranges available in this field, provide the opportunity to study the stellar populations and structural properties of galaxies beyond the cluster, as well as to discover rare astrophysical objects, such as compact massive galaxies and strong gravitational lenses (e.g., Tortora et al. 2018; Petrillo et al. 2017). The FDS image quality is similar to the one of the KiDS survey (Kuijken et al. 2019), since the longer exposures in FDS images are balanced by a slightly poorer seeing (*r*-band FWHM of ∼0.″9 for FDS, vs. ∼0.″65 in KiDS). The limiting magnitudes in the two surveys are quite similar, but the FDS is deeper in the *i*-band.

Taking advantage of the FDS data, we aim at determining photometric redshifts, stellar masses, galaxy classifications, and structural parameters of thousands of background galaxies. The goal is to provide a complete characterization of the background galaxy population over the area meant for investigating the evolution of the structural and stellar properties of galaxies as a function of redshift and mass. The tools for deriving all required quantities are already available and well-tested among our team (e.g., La Barbera et al. 2008; Cavuoti et al. 2017; Roy et al. 2018).

As a first test on the background galaxy population in FDS, we run a code to find galaxy-galaxy lens candidates. The code uses a machine learning classification method based on convolutional neural networks (CNNs), and was already applied to the KiDS survey (de Jong et al. 2017; Petrillo et al. 2019). We performed the run of CNN with a network trained on a large sample of *r*-band (or combined *g*-*r*-*i*) KiDS images, to the equivalent FDS images. Although the network is not customized and trained on FDS images, KiDS and FDS are based on data from the same telescope and camera, and, as mentioned above, are comparable in both FWHM and depth. Therefore, this is a valid approach to search gravitational lenses in FDS. In fact, we have already discovered several gravitational lens candidates in the FDS fields; two of them with FDS catalogue ID and coordinates: FDSJ032720.32-365821.81 at [51.834682; −36.972725] and FDSJ034739.60-352516.23 at [56.91502, −35.421176], which are presented in Fig. 18 as an example of the potential of this approach.

Fig. 18. Two example lens candidates found in the FDS fields applying the CNN code; the image cutout have 20.″0 side. *Left*: FDSJ032720.32-365821.81. *Right*: FDSJ034739.60-352516.23.

5. Conclusions

In this paper, we present the photometric and morphometric catalog of compact and slightly extended sources in the Fornax galaxy cluster, derived with VST observations within the FDS survey over an area of ∼21 square degrees in *ugri*-bands, and in *gri*-bands for a total of ∼27 square degrees.

The *ugri* data of FDS cover the main body of Fornax, centered on NGC 1399, and extend out to ∼1 Mpc, the virial radius of the cluster. The *gri* coverage, FDSex, extends to the South-West region of the Fornax A sub-cluster with its brightest galaxy, NGC 1316.

Because of the large FWHM variation from field to field, to improve the uniformity of sources detection and their morphological characterization, we derived a master-detection frame by coadding all *gri* single exposures with $FWHM \leq 0.''9$; starting from a median FWHM ranging from 0.″92 to 1.″26 with rms within 0.″11−0.″17 for the various bands, adopting the multi-band stacking procedure we ended up with a master-detection frame with a median FWHM of $0.''80 \pm 0.''04$, ∼15% improvement over the median FWHM of the highest resolution imaging (*r*-band), and a factor of ∼2.5 lower rms.

We calibrated the photometry using a two-step procedure, to reduce the effect of the independent calibration of the FDS fields, which generate a non-negligible photometric offset between neighboring fields. The first calibration step follows the standard calibration plan of VST frames. As a second step, we used the APASS photometry to derive a matrix to match the full FDS catalog to a unique reference. With this approach, the photometric offset between fields becomes negligible, and the re-calibrated photometry shows a general good match to existing literature data from SKyMapper, from the HST/ACSFCS survey and to predictions from stellar population synthesis models.

The catalogs are available through the project web pages, and will also be available on CDS. In the catalogs we provide the position, the photometry and the morphometry for 1.7 million sources with *ugri* detections, and for 3.1 million sources with *gri* data. As a preliminary use of the catalogs, we analysed

the 2-D distribution of compact stellar systems in the area, with particular attention given to GCs.

With the FDS instrumental setup and at the distance of Fornax, GCs are by all means point-like sources, except for a possible fraction of $\lesssim$0.5% of the population. Hence, GCs can be identified by their compactness.

To obtain the least contaminated GCs sample, we selected a number of morpho-photometric features and analysed them over a reference catalog of confirmed GCs and UCDs in Fornax. Such catalog is build by cross-matching the FDS catalogs with available spectroscopic and photometric datasets of confirmed GC/UCD. The reference catalog is then used to define the GCs loci in the parameter space, for the chosen photometric and morphometric parameters.

The GCs maps over the FDS area confirm the results of previous studies, about the presence of a large inter-galactic GC population around the main body of the cluster, centered on NGC 1399, stretched along the East-West direction. Here we find a small tilt of the distribution in the direction of NGC 1336 by ~10 deg. The distribution appears to extend over ~1 Mpc from side to side, highly flattened, with an ellipticity of ~0.65. In addition to our previous results, we find that one of the features already discussed, which extends from the main cluster body to the South-West direction, might be a tail of relatively blue GCs from NGC 1404, a bright galaxy close to the cluster core and with a peculiarly poor GCs population.

Of the GCs features already commented in the past, we here highlight the case of NGC 1336, which we confirm to be relatively isolated from the cluster, and with a high specific frequency of GCs; this might support the hypothesis that it is an infalling massive galaxy, with a GCs system that possibly experienced only few disruption processes. We also inspected the blue/red GCs maps, and confirm the known property of blue GCs residing in the wider cluster area, and red GCs being more concentrated on massive galaxies.

Systems selected to fit the color-magnitude range of spectroscopically confirmed UCDs show a substantial overdensity in the central cluster. The 160 UCD candidates are about three times more than the currently known UCDs in Fornax and would require spectroscopic follow up to learn more about their nature.

We also derived the GCs maps over the FDSex area, which has the disadvantage of suffering for larger contamination because of the lack of *u*-band over the NGC 1316 area, but has the advantage of covering this brightest cluster galaxy. With the caveat that the *gri* catalogs do not allow the detailed analysis allowed over the FDS area, despite our attempts to obtain a cleaner GC candidates sample, we do not find significative GCs structures along the NGC 1399–NGC 1316 direction, which extends over a projected distance of ~1.3 Mpc. This might be due to the lower efficiency of the GC identification. However, assuming similar contamination of the *gri* catalogs over the NGC 1399 and NGC 1316, we find that the GC population of the former outnumbers the second by a factor of ~4, and by about a factor of ~10 when normalized to galaxy luminosity, within a galactocentric range of 6′−24′, and remains a factor of ~3 higher than NGC 1316 at larger galactocentric radii, out to ~40′. Hence, the "contrast" of the GC populations towards NGC 1316 might be too low for the purpose of our study, – in spite of its luminosity twice larger than NGC 1399 – and might explain the difficulty in finding GCs sub-structures, which intrinsically need a large number of candidates over a given region to be identified. The rich intra-cluster GCs population around NGC 1399 does not seem to be matched by a similarly rich system around NGC 1316, the brightest galaxy of the Fornax A sub-cluster. In spite of this, the lack of obvious GC sub-structures between these two bright and massive galaxies might also be consequence of the NGC 1316 sub-cluster being in its first infalling phase and evolving autonomously, a result also supported by an independent analysis of FDS data for galaxy surface brightness profiles and intracluster light (Iodice et al. 2017b; Raj et al. 2019). A deeper analysis of the 2-D maps and other characteristics of the GCs over the FDS and FDSex area is in progress and will be presented in a dedicated paper.

Finally, we offer an example use of the catalogs for analyzing background galaxies. Using machine-learning methods, which have already been tested on the KiDS survey with VST, we identified two lens candidates in the FDS area.

Acknowledgements. This research was made possible through the use of the AAVSO Photometric All-Sky Survey (APASS), funded by the Robert Martin Ayers Sciences Fund and NSF AST-1412587. This work is based on visitor mode observations collected at the European Organisation for Astronomical Research in the Southern Hemisphere under the following VST GTO programs: 094.B-0512(B), 094.B-0496(A), 096.B-0501(B), 096.B-0582(A). INAF authors acknowledge financial support for the VST project (P.I. P. Schipani). We acknowledge the use of data from the SKyMapper survey. The national facility capability for SkyMapper has been funded through ARC LIEF grant LE130100104 from the Australian Research Council, awarded to the University of Sydney, the Australian National University, Swinburne University of Technology, the University of Queensland, the University of Western Australia, the University of Melbourne, Curtin University of Technology, Monash University and the Australian Astronomical Observatory. SkyMapper is owned and operated by The Australian National University's Research School of Astronomy and Astrophysics. The survey data were processed and provided by the SkyMapper Team at ANU. The SkyMapper node of the All-Sky Virtual Observatory (ASVO) is hosted at the National Computational Infrastructure (NCI). Development and support the SkyMapper node of the ASVO has been funded in part by Astronomy Australia Limited (AAL) and the Australian Government through the Commonwealth's Education Investment Fund (EIF) and National Collaborative Research Infrastructure Strategy (NCRIS), particularly the National eResearch Collaboration Tools and Resources (NeCTAR) and the Australian National Data Service Projects (ANDS). MP acknowledges financial contribution from the agreement ASI-INAF n.2017-14-H.O. JFB acknowledges support through the RAVET project by the grant AYA2016-77237-C3-1- P from the Spanish Ministry of Science, Innovation and Universities (MCIU) and through the IAC project TRACES which is partially supported through the state budget and the regional budget of the Consejería de Economía, Industria, Comercio y Conocimiento of the Canary Islands Autonomous Community. GvdV acknowledges funding from the European Research Council (ERC) under the European Union's Horizon 2020 research and innovation programme under grant agreement No 724857 (Consolidator Grant ArcheoDyn). CT acknowledges funding from the INAF PRIN-SKA 2017 program 1.05.01.88.04.

References

Alam, S., Albareti, F. D., Allende Prieto, C., et al. 2015, ApJS, 219, 12
Alamo-Martínez, K. A., Blakeslee, J. P., Jee, M. J., et al. 2013, ApJ, 775, 20
Angora, G., Brescia, M., Cavuoti, S., et al. 2019, MNRAS, 490, 4080
Ashman, K. M., & Zepf, S. E. 1992, ApJ, 384, 50
Bastian, N., & Lardo, C. 2018, ARA&A, 56, 83
Bekki, K., Forbes, D. A., Beasley, M. A., & Couch, W. J. 2003, MNRAS, 344, 1334
Bergond, G., Athanassoula, E., Leon, S., et al. 2007, A&A, 464, L21
Bertin, E., & Arnouts, S. 1996, A&AS, 117, 393
Blakeslee, J. P., Jordán, A., Mei, S., et al. 2009, ApJ, 694, 556
Blakeslee, J. P., Cantiello, M., & Peng, E. W. 2010, ApJ, 710, 51
Bournaud, F. 2011, in EAS Publications Series, eds. C. Charbonnel, & T. Montmerle, EAS Publ. Ser. , 51, 107
Brocato, E., Castellani, V., Raimondo, G., & Romaniello, M. 1999, A&AS, 136, 65
Brodie, J. P., & Strader, J. 2006, ARA&A, 44, 193
Cantiello, M. 2016, The Universe of Digital Sky Surveys, eds. N. R. Napolitano, G. Longo, M. Marconi, M. Paolillo, & E. Iodice, 42, 157
Cantiello, M., Raimondo, G., Brocato, E., & Capaccioli, M. 2003, AJ, 125, 2783
Cantiello, M., Blakeslee, J. P., Raimondo, G., et al. 2014, A&A, 564, L3
Cantiello, M., Capaccioli, M., Napolitano, N., et al. 2015, A&A, 576, A14
Cantiello, M., D'Abrusco, R., Spavone, M., et al. 2018a, A&A, 611, A93
Cantiello, M., Grado, A., Rejkuba, M., et al. 2018b, A&A, 611, A21

Carretta, E., Bragaglia, A., Gratton, R. G., et al. 2009, A&A, 505, 117
Cavuoti, S., Amaro, V., Brescia, M., et al. 2017, MNRAS, 465, 1959
D'Abrusco, R., Cantiello, M., Paolillo, M., et al. 2016, ApJ, 819, L31
de Jong, J. T. A., Verdoes Kleijn, G. A., Kuijken, K. H., & Valentijn, E. A. 2013, Exp. Astron., 35, 25
de Jong, J. T. A., Kleijn, G. A. V., Erben, T., et al. 2017, A&A, 604, A134
Durrell, P. R., Côté, P., Peng, E. W., et al. 2014, ApJ, 794, 103
Fahrion, K., Georgiev, I., Hilker, M., et al. 2019a, A&A, 625, A50
Fahrion, K., Lyubenova, M., van de Ven, G., et al. 2019b, A&A, 628, A92
Ferguson, H. C. 1989, AJ, 98, 367
Ferrarese, L., Côté, P., Cuillandre, J.-C., et al. 2012, ApJS, 200, 4
Firth, P., Drinkwater, M. J., Evstigneeva, E. A., et al. 2007, MNRAS, 382, 1342
Gómez, M., Richtler, T., Infante, L., & Drenkhahn, G. 2001, A&A, 371, 875
Goudfrooij, P., Mack, J., Kissler-Patig, M., Meylan, G., & Minniti, D. 2001, MNRAS, 322, 643
Gregg, M. D., Drinkwater, M. J., Evstigneeva, E., et al. 2009, AJ, 137, 498
Hilker, M., Baumgardt, H., Infante, L., et al. 2007, A&A, 463, 119
Iodice, E., Capaccioli, M., Grado, A., et al. 2016, ApJ, 820, 42
Iodice, E., Spavone, M., Cantiello, M., et al. 2017a, ApJ, 851, 75
Iodice, E., Spavone, M., Capaccioli, M., et al. 2017b, ApJ, 839, 21
Iodice, E., Spavone, M., Capaccioli, M., et al. 2019, A&A, 623, A1
Ivezić, Ž., Lupton, R. H., Schlegel, D., et al. 2004, Astron. Nachr., 325, 583
Janssens, S., Abraham, R., Brodie, J., et al. 2017, ApJ, 839, L17
Jedrzejewski, R. I. 1987, MNRAS, 226, 747
Johnston, K. V., Bullock, J. S., Sharma, S., et al. 2008, ApJ, 689, 936
Jordán, A., McLaughlin, D. E., Côté, P., et al. 2007, ApJS, 171, 101
Jordán, A., Peng, E. W., Blakeslee, J. P., et al. 2009, ApJS, 180, 54
Jordán, A., Peng, E. W., Blakeslee, J. P., et al. 2015, ApJS, 221, 13
Kim, H.-S., Yoon, S.-J., Sohn, S. T., et al. 2013, ApJ, 763, 40
Kissler-Patig, M., Grillmair, C. J., Meylan, G., et al. 1999, AJ, 117, 1206
Kron, R. G. 1980, ApJS, 43, 305
Kuijken, K. 2011, The Messenger, 146, 8
Kuijken, K., Heymans, C., Dvornik, A., et al. 2019, A&A, 625, A2
La Barbera, F., de Carvalho, R. R., Kohl-Moreira, J. L., et al. 2008, PASP, 120, 681
Larsen, S. S. 1999, A&AS, 139, 393
Liu, Y., Peng, E. W., Jordán, A., et al. 2019, ApJ, 875, 156
Masters, K. L., Jordán, A., Côté, P., et al. 2010, ApJ, 715, 1419
McFarland, J. P., Verdoes-Kleijn, G., Sikkema, G., et al. 2013, Exp. Astron., 35, 45
Mentz, J. J., La Barbera, F., Peletier, R. F., et al. 2016, MNRAS, 463, 2819
Mieske, S., Hilker, M., & Infante, L. 2004, A&A, 418, 445
Mieske, S., Hilker, M., Jordán, A., et al. 2008, A&A, 487, 921
Mieske, S., Hilker, M., & Misgeld, I. 2012, A&A, 537, A3
Misgeld, I., & Hilker, M. 2011, MNRAS, 414, 3699
Mo, H., van den Bosch, F. C., & White, S. 2010, Galaxy Formation and Evolution (Cambridge University Press)
Muñoz, R. P., Puzia, T. H., Lançon, A., et al. 2014, ApJS, 210, 4
Onken, C. A., Wolf, C., Bessell, M. S., et al. 2019, PASA, 36, e033
Paolillo, M., Fabbiano, G., Peres, G., & Kim, D.-W. 2002, ApJ, 565, 883
Pedregosa, F., Varoquaux, G., Gramfort, A., et al. 2011, J. Mach. Learn. Res., 12, 2825
Peng, E. W., Jordán, A., Côté, P., et al. 2006, ApJ, 639, 95
Peng, E. W., Ferguson, H. C., Goudfrooij, P., et al. 2011, ApJ, 730, 23
Petrillo, C. E., Tortora, C., Chatterjee, S., et al. 2017, MNRAS, 472, 1129
Petrillo, C. E., Tortora, C., Chatterjee, S., et al. 2019, MNRAS, 482, 807
Piotto, G., Bedin, L. R., Anderson, J., et al. 2007, ApJ, 661, L53
Pota, V., Napolitano, N. R., Hilker, M., et al. 2018, MNRAS, 481, 1744
Puzia, T. H., Paolillo, M., Goudfrooij, P., et al. 2014, ApJ, 786, 78
Raimondo, G., Brocato, E., Cantiello, M., & Capaccioli, M. 2005, AJ, 130, 2625
Raj, M. A., Iodice, E., Napolitano, N. R., et al. 2019, A&A, 628, A4
Roy, N., Napolitano, N. R., La Barbera, F., et al. 2018, MNRAS, 480, 1057
Schipani, P., D'Orsi, S., Fierro, D., & Marty, L. 2010, Appl. Opt., 49, 3199
Schlafly, E. F., & Finkbeiner, D. P. 2011, ApJ, 737, 103
Schlegel, D. J., Finkbeiner, D. P., & Davis, M. 1998, ApJ, 500, 525
Schuberth, Y., Richtler, T., Hilker, M., et al. 2010, A&A, 513, A52
Sesto, L., Faifer, F., Forte, J., & Smith Castelli, A. 2017, Galaxies, 5, 39
Sheardown, A., Roediger, E., Su, Y., et al. 2018, ApJ, 865, 118
Spavone, M., Capaccioli, M., Napolitano, N. R., et al. 2017, A&A, 603, A38
Spiniello, C., Napolitano, N. R., Arnaboldi, M., et al. 2018, MNRAS, 477, 1880
Stetson, P. B. 1987, PASP, 99, 191
Su, Y., Nulsen, P. E. J., Kraft, R. P., et al. 2017, ApJ, 851, 69
Tortora, C., Napolitano, N. R., Spavone, M., et al. 2018, MNRAS, 481, 4728
Usher, C., Forbes, D. A., Brodie, J. P., et al. 2012, MNRAS, 426, 1475
Vanzella, E., Calura, F., Meneghetti, M., et al. 2017, MNRAS, 467, 4304
Venhola, A., Peletier, R., Laurikainen, E., et al. 2017, A&A, 608, A142
Venhola, A., Peletier, R., Laurikainen, E., et al. 2018, A&A, 620, A165
Venhola, A., Peletier, R., Laurikainen, E., et al. 2019, A&A, 625, A143
Villegas, D., Jordán, A., Peng, E. W., et al. 2010, ApJ, 717, 603
West, M. J., Côté, P., Marzke, R. O., & Jordán, A. 2004, Nature, 427, 31
Wittmann, C., Kotulla, R., Lisker, T., et al. 2019, ApJS, 245, 10
Wolf, C., Onken, C. A., Luvaul, L. C., et al. 2018, PASA, 35, e010
Yoon, S.-J., Yi, S. K., & Lee, Y.-W. 2006, Science, 311, 1129